Precision measurements on lithium atoms in an electric field compared with *R*-matrix and other Stark theories

G. D. Stevens, C.-H. Iu, T. Bergeman, and H. J. Metcalf
Physics Department, State University of New York, Stony Brook, New York 11794-3800

I. Seipp* and K. T. Taylor
School of Mathematics and Physics, The Queen's University of Belfast, Belfast BT7 1NN, Northern Ireland

D. Delande
Laboratoire Kastler-Brossel, Université Pierre et Marie Curie, 4 place Jussieu, 75005 Paris, France
(Received 14 August 1995)

We have made careful measurements of Stark resonances in ^{7}Li Rydberg states above and below the classical saddle point to test various theories and to obtain a precise calibration of the electric field. Rydberg states were populated by two-step diode laser excitation to the $3\,^2S$ state followed by He-Ne or diode laser excitation to Stark sublevels near the $n=15$ manifold energy. Calibration was performed by comparing measured resonance positions with theoretical results. For zero-field energies, the theoretical calculations were made using quantum defect parameters obtained by fitting available spectral data on Li, and from recent polarization model results of Drachman and Bhatia [Phys. Rev. A **51**, 2926 (1995)]. Three theoretical methods were used: (1) matrix diagonalization over a basis of spherical coordinate states, for which the precision declines as one approaches the saddle point; (2) frame transformation theory, which makes very economical use of computer resources but is not reliable beyond a precision of about 500 ppm in an electric field; (3) a recently developed *R*-matrix method. The last of these was most accurate and, like the second, could be used both below and above the saddle point. From the measured resonance positions and an optimum set of Li quantum defect parameters, the *R*-matrix calculations provided a calibration of the electric field to about $\pm$ 2 ppm ± 4 mV/cm. We briefly discuss certain refinements and shortcomings of the other two theoretical methods, and the special procedures used to obtain high accuracy with the *R*-matrix method.

PACS number(s): 32.60.+i, 32.10.Dk, 31.15.−p, 41.20.−q

I. INTRODUCTION

In principle, it is possible to calibrate a static electric field to the accuracy of the relevant fundamental constants (currently ~ 0.3 ppm) by measuring resonances of simple atoms in electric fields and comparing with theoretical results. A calibration standard is needed for precision measurements of atomic polarizabilities and molecular dipole moments, and for testing Stark theory in various atoms. Measurements of atomic Rydberg levels in an electric field have also been used to map spatial variations of electrostatic fields [1], and a calibration standard would provide an absolute scale. In addition, measurements of the Stark effect have been used to measure binding energies [2] and energy differences [3] of the lower states of a laser-induced transition.

For alkali-metal atoms, neither the theoretical nor experimental techniques have been tested previously at the ppm level of precision. The theory of hydrogen atoms in an electric field is presumed known to high accuracy [4–6], but because of special requirements and circumstances (dissociation of H_2 into H atoms, excitation, and fast beam velocities) precision experiments on hydrogen have not been reported. Therefore Stark measurements on atoms with one electron outside a closed shell are of interest both for testing theories for nonseparable quantum systems and for precision field calibration. Previously, the most precise electric-field calibration appears to be about $\pm$ 50 ppm from measurements on excited helium atoms [7]. In contrast, magnetic fields can be calibrated to much better than 1 ppm by NMR techniques.

In hopes of achieving a precision electric-field calibration with Rb atoms, measurements of resonance narrowings above the saddle point $E=-2\sqrt{F}$ were made by Yang *et al.* some years ago [1]. Resonance narrowing occurs when two or more energy levels couple in such a way that different decay channels interfere. It can dramatically increase the lifetime of one of the states over a small range of field [8–11]. Such a sharp feature would appear to be well suited for field calibration experiments. The data from the Rb experiments were compared with computational results from Harmin's frame transformation (FT) theory [12–14] to give an absolute calibration. Unfortunately, there were inconsistencies as large as 1000 ppm in the calibration parameters obtained from different narrowing regions. One possible explanation for the discrepancies was that the large and polarizable Rb ion core was not properly taken into account in the theory. If so, then a lighter alkali-metal atom would be expected to provide better agreement. For the present experiments, we selected Li, which had previously been used for comparisons between precision measurements and theory for the diamagnetic Zeeman effect [15,16].

Initial measurements showed that the change from Rb to Li did not alleviate the discrepancies, and it became clear

* Permanent address: Theoretische Astrophysik, Universität Tübingen, Auf der Morgenstelle 10, D 72076 Tübingen, Germany.

that such inaccuracies were inherent in the FT computational method, applied either below or above the saddle point. Shortly after this conclusion was reached, an alternative theory for atoms in an electric field was developed [17] using R-matrix methods [16,18]. In the present work, we report corroboration between Stark measurements on lithium atoms and R-matrix calculations at the level of about 2 ppm. This level of precision is approximately 80 times better than that achieved in the study of the diamagnetic Zeeman effect in Li Rydberg levels [15,16]. A summary of the present work has recently been published [19].

The theory of the Stark effect in nonhydrogenic atoms presents a special type of nonseparable partial differential equation for the outer electron. The core region must be effectively excised from the solution since it constitutes a many-body problem. Within and near the core, the external electric field is negligible compared with the internal atomic field and the problem is nearly spherically symmetric. Outside the core itself, core effects can be expressed to a high degree of accuracy by the l-dependent quantum defect phase shifts, as discussed in Sec. III. Neglecting core polarization effects, the outer region is separable in parabolic coordinates.

The theoretical methods discussed here take three different strategies for modeling the core and the outer region. In the matrix diagonalization (MD) method [20] (Sec. IV), the electric field is the perturbing element. The basis functions are zero-field eigenfunctions for various n,l states, with energies given by a quantum defect expansion, hence with the correct phase shift outside the core region. This method is limited because only bound states are included in the basis set. To obtain convergence as the field approaches the saddle point at a given energy, progressively larger basis sets must be used, but spurious resonances can occur when high-lying basis states are Stark shifted all the way down into the region of interest. In an attempt to estimate shifts due to high-n levels and the continuum, we extrapolate calculated energies as a function of the uppermost energy of the basis set (see Sec. IV). This results in a modest improvement of MD energies, but does not attain the desired level of accuracy.

The frame transformation method [12–14] (Sec. V) uses parabolic coordinate solutions for the outer region. Each parabolic channel wave function is decomposed into spherical components, to which the appropriate l-dependent phase shift is applied. In the original formulation [12,13], WKB wave functions were used. We have substituted numeric wave functions, and found slightly improved comparisons with experiment, shown in Sec. VIII. In Secs. V and VIII, we speculate on the origin of the discrepancies observed when comparing FT results with experiment.

Finally, the R-matrix (RM) approach [16–18,21] (Sec. VI) matches the phase-shifted spherical wave functions at a radius $r=a$ with eigenfunctions of the hydrogenic atom plus electric field system at large r. These eigenfunctions are computed as combinations of spherical coordinate Sturmian functions. Complex coordinates and energies are used to achieve square integrability. The Sturmian functions provide this method with great flexibility to match both the boundary conditions at $r=a$ and the desired long-range behavior.

Our experimental technique employed a three-photon stepwise excitation of ^{7}Li from the $2\,^2S_{1/2}$ ground state via the $2\,^2P_{3/2}$ to the $3\,^2S_{1/2}$ state and then to Stark sublevels

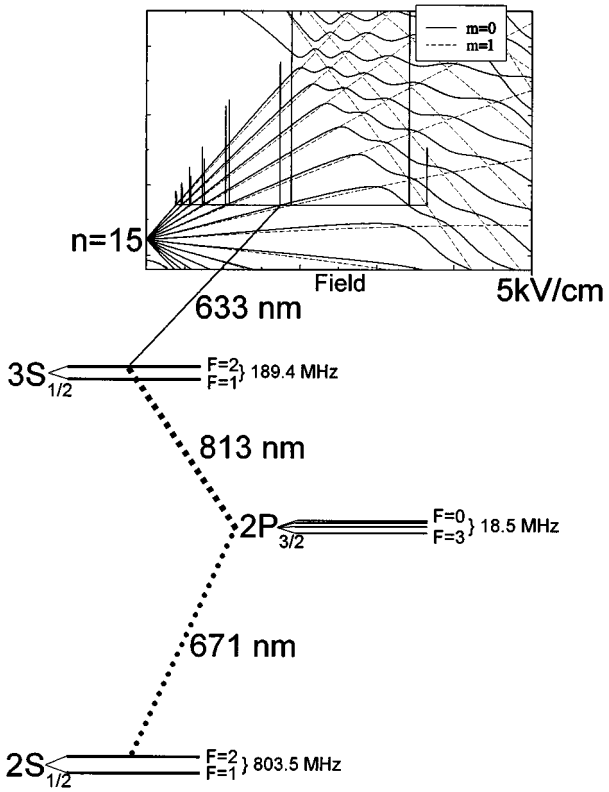

FIG. 1. Excitation scheme used in these experiments. A representative field scan is overlaid on the Stark manifold around $n=15$ as a visual aid.

near the $n=15$ manifold energies (see Fig. 1). As in the experiments on rubidium (where decay times were measured with pulsed laser excitation), we have made some measurements of interference narrowing, but of the resonance linewidths rather than decay rates (Sec. VII). With cw lasers, however, it is more precise and convenient to measure electric-field values of successive Stark resonances at fixed laser frequency. This spectroscopic method also is advantageous relative to lifetime measurements because it is sensitive to field variations only over the excitation region, not over the entire decay length, and because measurements can be made below the saddle point, where MD calculations [20] provide a useful first approximation. In addition, the resonances occur at any energy and do not require a search procedure, as needed to locate regions of interference narrowing. Data were obtained with a stabilized diode laser or He-Ne laser exciting from the $3\,^2S_{1/2}$ state, by scanning the electric field. Resonance peak positions below and above the saddle point were measured. Further details of the experiment are discussed in Sec. II.

In Sec. VIII we present fits of spectroscopic measurements to computational results from the R-matrix method. The field calibration exhibits an uncertainty of about 2 ppm in the effective electrode plate separation plus an uncertainty of 4 mV/cm from the voltage offset parameter. The fitted energy of the upper levels excited by the third laser has an uncertainty of about 1.5 MHz. These error estimates include effects of uncertainties in the quantum defect parameters, as discussed in Sec. VIII. In Sec. VIII we also show that MD eigenvalues typically exhibit systematic errors, and FT results are again off by a large amount. In the Appendix, atomic units of energy and field are discussed.

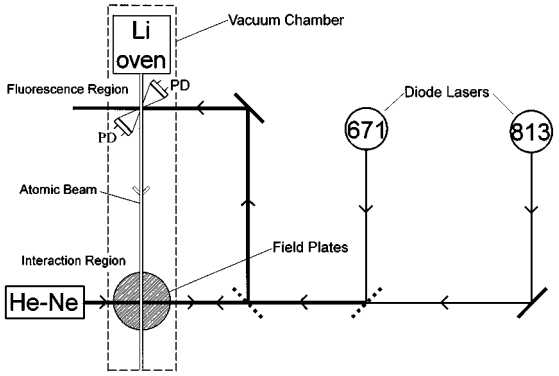

FIG. 2. A schematic of our experimental apparatus showing the geometry of the three excitation lasers with respect to the atomic beam.

II. EXPERIMENTAL SETUP

Our three-step excitation scheme utilizes a $\lambda = 670$-nm diode laser to excite from $2\,^2S_{1/2} \rightarrow 2\,^2P_{3/2}$, a $\lambda = 813$-nm diode laser to excite $2\,^2P_{3/2} \rightarrow 3\,^2S_{1/2}$, and a third laser, at $\lambda = 633$ nm, to excite from $3\,^2S_{1/2}$ to $n=15$ states (see Fig. 1) [22]. The first two lasers are locked to atomic resonances in the (field-free) fluorescence region of our apparatus (see Fig. 2), while the third laser, either a diode laser or He-Ne laser, is frequency stabilized using different schemes. The diode laser is stabilized by locking to an Invar Fabry-Pérot reference cavity. This cavity is kept in rough vacuum to minimize environmental thermal and pressure effects and provides an overall frequency stability of approximately 1 MHz/h. The He-Ne laser is stabilized by locking to a difference signal from the two stable laser cavity modes of perpendicular polarizations (polarization stabilization).

Rydberg states near the $n=15$ manifold energy are populated by scanning the electric field in the interaction region (Fig. 2) to shift the Stark levels into resonance with the 633-nm light for transitions from $3\,^2S_{1/2}(F=2)$. The population of Rydberg atoms is measured by collecting ions through a slit in the bottom field plate, amplifying this ion signal with two microchannel plates and a home-built preamplifier, and counting the resulting pulses by computer. A scan over a wide field region is superimposed on a plot of lithium levels in an electric field in Fig. 3. The He-Ne laser is linearly polarized at roughly 45° from the electric-field direction. Therefore the three series $m=-1,0,1$ are excited in our experiment. Because of time-reversal invariance, $m=1$ and $m=-1$ levels are degenerate. We thus measure in a single scan two independent series of energy levels, $m=0$ and $|m|=1$.

Our signal detection scheme differs from other Rydberg experiments in that the atoms are ionized directly by the applied field or photoionized by absorbing additional laser photons or blackbody radiation. Since no pulsed field is needed, we are able to measure plate potentials with excellent accuracy using a stable voltage divider. The divider used in our experiment consists of five 20-MΩ and one 30-KΩ Caddock MG815 resistors. It is used in conjunction with a Keithley Model 196 DMM (digital multimeter) (0.83 ppm/h accuracy) to measure the top plate's potential ranging from 0 to 10 kV, which is recorded at the beginning and end of data acquisition via a general purpose interface bus (GPIB) interface. This potential is applied using a Spellman RHSR series high voltage dc supply that has an overall stability of about 1 ppm/min (see additional comments on this in Sec. VIII). The field is scanned and recorded remotely by a computer that changes the bottom field plate potential from 0 to 10 V. This scanning voltage is also calibrated using the same precision voltage divider used to determine the top plate's potential so that only one calibration factor is involved in the determination of the potential difference of the plates.

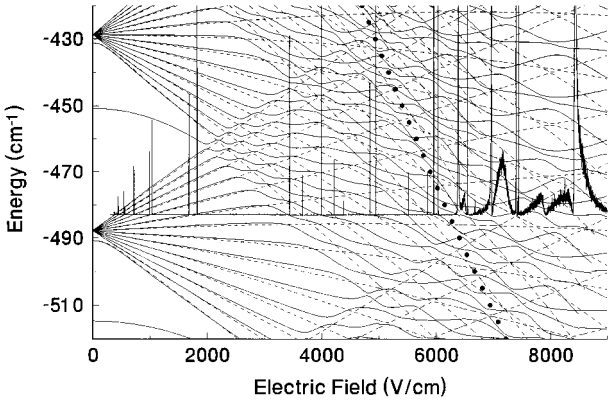

FIG. 3. Data obtained from a scan at $-483.06\ \mathrm{cm}^{-1}$ excitation energy from 1 to 9 kV/cm overlaid on a plot of Li energy levels. Solid lines denote $m=0$ levels, dashed lines $|m|=1$ levels, and dots denote the saddle-point energy. Eigenvalues above the saddle point have been computed with a multichannel Fano resonance adaptation of FT theory [23,24]. The plotted energies terminate at the local parabolic critical field [5]. Broad resonances occur near and beyond each of these points.

We determine the center location of each resonance by fitting the ionization signal to a Gaussian function. This function closely approximates the sub-saddle-point experimental line profile, which is a Doppler broadened convolution of the natural and laser line shapes. On a frequency scale, these resonances have typical linewidths of about 30 MHz. A typical scan over a resonance is shown in Fig. 4, which also shows the fitted Gaussian function and the peak center with error bars. The experimental line shape in this figure exhibits some asymmetry that we attribute to small drifts of the power supply voltage and of the laser frequencies. Since these drifts are random, it would not be appropriate to intro-

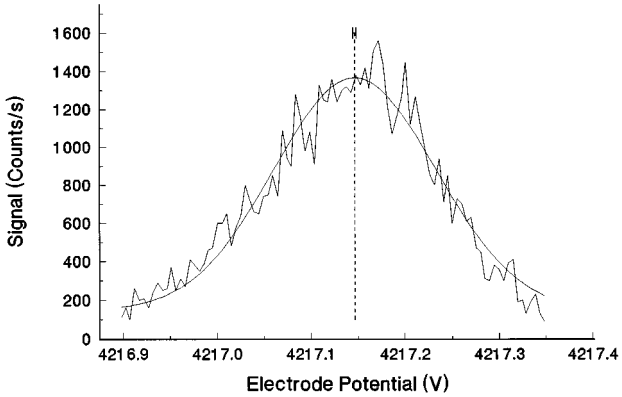

FIG. 4. Data from a scan over an individual resonance peak together with the fitted Gaussian function. The fitted resonance voltage and error limits are also shown.

duce an asymmetry parameter into the line shape fit. However, because of this situation, the error bars as given in this figure (standard deviations returned by the fitting program) are typically too small by a factor of 3 to 10. The scatter of experimental points in the global fit (Sec. VIII) is a truer measure of the actual uncertainties in the resonance peak positions.

Peaks at higher fields exhibit larger linewidths that scale with field as a result of field inhomogeneities arising from the slit in the bottom field plate. Above the saddle point, resonance line shapes, especially for $m=0$ peaks, broaden further and become distinctly asymmetric. These may be described by Fano profiles, reflecting core-induced coupling of discrete states with the continuum. In general, we did not attempt to fit the centers of such broadened resonances since it would not have improved the field calibration.

III. QUANTUM DEFECT PARAMETERS

For the Stark theory calculations, accurate zero-field energies are needed, particularly for $n=15$ levels. The accuracy required is indicated by the uncertainty given in Sec. VIII, which is about 1 MHz. There have been few direct measurements of $n=15$ levels in Li, and *ab initio* theory is not yet sufficiently accurate. Therefore, for $l\leqslant 3$, the energies needed for the calculations have been obtained from quantum defect (QD) parameters fitted to experimental data. The QD expansion effectively provides an interpolation between microwave data on high-n levels and optical data on low-n levels. For $l\geqslant 4$, the QD parameters are obtained from the polarization model [25] (including relativistic terms). We now define our quantum defect parameters, explain how we fit them from the zero-field data, discuss the polarization model and relativistic terms, and give the resulting parameters.

The quantum defect expansion of atomic energy levels, attributed to Ritz [26], was shown by Hartree [27] to be valid for any spherically symmetric perturbing potential of finite range. Drake and Swainson [28] have recently verified Hartree's theorem for an expansion of the form originally used by Ritz. Namely, energies are written

$$E(n,L)=-R_A/(n-\mu)^2, \tag{1}$$

where here $R_A=R_{^7\mathrm{Li}}$ is the Li Rydberg constant, as given in the Appendix, and

$$\mu=\mu_0+\frac{\mu_2}{(n-\mu)^2}+\frac{\mu_4}{(n-\mu)^4}+\cdots. \tag{2}$$

Since the quantum defect μ occurs in the denominators, iteration must be used to determine μ for any integral n value. For intermediate energies E such as occur in the Stark effect, Eq. (2) is a simple series in E/R_A, with even powers only. All core effects can be represented by the above expansion.

For sufficiently high l, penetration and exchange effects are negligible, and one can compute the needed quantum defects from core polarization and relativistic effects. Drachman and Bhatia [25] have used accurate correlated wave functions for the Li ion core to calculate the polarizabilities and adiabatic corrections required for terms up to r^{-8}. Their resultant potential may be written (in atomic units)

TABLE I. Polarization model parameters from Ref. [25] as used in this work.

c_4	-0.19248540
c_6	0.097881
c_7	0.143125
c_8	$-0.428584+0.049005l(l+1)$

$$U_{\mathrm{pol}}=\frac{1}{2}\left[U_4+U_6+\frac{1}{2}(U_7+U_8)\pm\frac{1}{2}(U_7+U_8)\right], \tag{3}$$

where $U_n=c_n/r^n$. Values for c_n from Ref. [25] are given in Table I. Since the series is asymptotic, the uncertainty is taken to be equal in magnitude to the last term (U_7 and U_8 are mathematically related).

Relativistic effects have a slightly different form. Although spin-orbit effects are negligible in this work, the relativistic mass correction is significant. The (weighted) average shift for the $J=l\pm 1/2$ components of a given n,l level from Dirac's theory for hydrogen is

$$\Delta E_{\mathrm{rel}}=\frac{\alpha^2 R_A}{n^3}\left(\frac{3}{4n}-\frac{2}{2l+1}\right). \tag{4}$$

(For S states, $l=1/2$ is to be substituted.) The shift varies between 52 and 1 MHz for $n=15$ levels, $l=0$ to 14, respectively. The n^{-3} term in Eq. (4) may be combined with the μ_0 term in the Ritz expansion. In principle, the n^{-4} term deviates from the Ritz expansion, and Drake [29] has recommended that this term be subtracted from the term energies before fitting quantum defect parameters. However, for $l\leqslant 3$, the present experimental uncertainties in the spectral data for Li happen to be larger than the n^{-4} term.

The polarization model and relativistic terms [25] have been confirmed to a high degree of precision by recent measurements of microwave transitions between $n=10$, $l=4$ to 6 levels [30]. We therefore assume that quantum defects for $l=4$ to 14 may be obtained to sufficient accuracy from this model.

To obtain quantum defect parameters for $l=0$ to 3, we have collected all available data on zero-field transitions between Li energy levels and fit them to expressions of the form of Eqs. (1) and (2). Specifically, the fitted data include recent interferometric measurements of the Li D lines [31], recent hollow cathode measurements on transitions between levels up to $n=7$ [32], earlier hollow cathode measurements [33], microwave measurements on ^2S and ^2P levels [34], microwave measurements on $^2D\rightarrow{}^2F$ and $^2D\rightarrow{}^2G$ (from Stark mixing) intervals [35], and unpublished laser spectroscopy measurements of $3\,^2S\rightarrow n\,^2P$ transitions [36]. In order to include $^2D\rightarrow{}^2G$ microwave data, polarization model results were used for the ^2G level energies. All these data sets were combined with weights appropriate to the measuring uncertainties in a simultaneous fit to ^2S, ^2P, ^2D, and ^2F quantum defect parameters. Fine structure parameters for each of these manifolds were fit but are not given here because they were not significant in the present measurements.

Table II gives the parameters obtained from the fit to the zero-field spectral data. For the optimum fit, referred to as fit A in Table II and elsewhere, the variance (rms ratio of re-

TABLE II. Quantum defect parameters for ^{7}Li obtained by fitting spectral data to Eqs. (1) and (2), Sec. III. QD set A has one more parameter for each l manifold than set B. The values for $E(n=15)$ are in cm^{-1}.

	^2S	^2P	^2D	^2F
		Fit A: Variance = 2.8		
μ_0	0.39951183	0.04716876	0.00194211	0.00030862
μ_2	0.02824560	−0.02398188	−0.00376875	−0.00099057
μ_4	0.02082123	0.01548488	−0.01563348	−0.00739661
μ_6	−0.09793152	−0.16065777	0.10335313	
μ_8	0.14782202	0.33704280		
$E(15)$	−514.74665	−490.75812	−487.80850	−487.70305
		Fit B: Variance = 9.2		
μ_0	0.39950971	0.04716701	0.00194961	0.00031432
μ_2	0.02900322	−0.02318304	−0.00452170	−0.00148768
μ_4	0.00532119	−0.00423309	0.00213012	
μ_6	−0.00502291	−0.00881455		
$E(15)$	−514.74673	−490.75812	−487.80879	−487.70329

siduals to estimated experimental uncertainties) was 2.8. For fit B there was one less parameter for each manifold, and the variance increases to 9.2. In view of the correlation between different parameters, it is necessary to retain several digits beyond the actual error limits to reproduce the input transition energies. The effect of uncertainties in the parameters in Table II on the Stark theory calculations is discussed in Sec. VIII.

Table III gives the QD parameters for $4 \leqslant l \leqslant 8$ obtained from the polarization model and relativistic effect [Eq. (4)], from expressions for r^{-n}, and from the corresponding contributions to $\mu_0, \mu_2 \ldots$, given in Eqs. (17)–(20) in Ref. [28]. Note that because of the contribution from $\Delta E_{\rm rel}$, the values do not decrease as l^{-5} (for $l \gg 1$) as otherwise expected.

IV. MATRIX DIAGONALIZATION

The historically oldest method we have used to calculate low-field resonance locations is based on Zimmerman's matrix diagonalization method [20], which is an extension of Schrödinger's original perturbation treatment of the Stark effect [37]. Matrix elements of the Stark term $Fz = Fr\cos\theta$ are calculated using zero-field spherical wave functions as basis states. We use the standard expressions for $\Delta l = \pm 1$ matrix elements of $\cos\theta$ in evaluating the angular integrals. The radial integrals are done using the Numerov technique [38] for the radial Schrödinger equation, with the variable $u = \sqrt{r}$ [39]. The integration begins at large u at the quantum defect energy of each state [40]. For l values for which the quantum defect shifts are negligible, we use Gordon's transition strength formula in terms of hypergeometric functions [41]. By setting the appropriate quantum defects equal to zero, the numeric integration results were confirmed by the hypergeometric function expressions to at least eight digits.

TABLE III. Quantum defect parameters for ^{7}Li obtained from the polarization model of Ref. [25].

l	μ_0	μ_2
4	8.861×10^{-5}	-5.47×10^{-4}
5	3.469×10^{-5}	-2.98×10^{-4}
6	1.690×10^{-5}	-1.79×10^{-4}
7	9.768×10^{-6}	-1.16×10^{-4}

However, this diagonalization method is limited by the necessarily finite basis set of bound states. Even though the assumed field may be less than the saddle-point value for the n level under consideration, it may be larger than the saddle point for a high-lying n,l basis state, and spurious resonances can occur when the high-lying states are shifted down into the region of interest. To simulate the extension of a basis set to higher-n levels and continuum states, we have extrapolated the calculated energies as a function of $E_{\rm max}$, the zero-field energy of the uppermost level of the basis set. In Ref. [3] an exponential form was used. We have since found that a power law of the form

$$E(E_{\rm max}) = E_\infty + \frac{A}{(E_{\rm max} - E_\infty)^\beta} \tag{5}$$

is more accurate. Here $E(E_{\rm max})$ are the calculated MD results and E_∞ is the extrapolated value that includes an estimate of shifts from higher-n levels and from the continuum. As discussed in Sec. VIII, for each resonance, E_∞ and A are found by least squares fit to a series of 12 to 15 values of $E(E_{\rm max})$. An optimum value $\beta = 2.50$ was found by using the MD approach and Eq. (5) for hydrogen $n=15$ levels. This is strictly an *ad hoc* empirical result. For the H 1 ^2S ground state, Eq. (5) does not apply. Values of $|\langle 1s|z|np\rangle|^2$ decrease as n^{-3} [42] while the $n\,^2P$ energy level spacings also decrease as n^{-3}, so $E(E_{\rm max})$ decreases approximately linearly with $E_{\rm max}$ for $E_{\rm max} \leqslant 0$. The extension of the function $E(E_{\rm max})$ for the H 1 ^2S state into the continuum has a rather complicated dependence on $E_{\rm max}$ [43], but eventually yields a 19% continuum contribution to the H 1 ^2S polarizability. We have not attempted such an analysis for the $n=15$ Stark sublevels. However, E_∞ values from MD calculations and Eq. (5) with $\beta = 2.5$ did produce agreement to within a few MHz of the "exact" energies for $n=15$ levels of hydrogen that we have obtained by the numeric method of Luc-Koenig

and Bachelier [5] and confirmed by calculations [44] with recently developed complex pole theory [4]. Extrapolated values for E_∞ from MD calculations for $n=15$ Li levels will be compared with RM results in Sec. VIII. To our knowledge, this represents the most precise application of the MD approach to Rydberg Stark levels.

V. FRAME TRANSFORMATION METHOD

In this section we present a brief review of Harmin's frame transformation Stark effect theory [12–14], and indicate how we incorporated numerical results to test the accuracy of the WKB approximations.

For hydrogen atoms in an electric field, the Schrödinger equation at energy ϵ [see Eq. (A3)] is separable in parabolic coordinates, $\xi=r+z$, $\eta=r-z$, and $\phi=\tan^{-1}(y/x)$:

$$\frac{d^2\chi^{\epsilon F}_{1n_1m}(\xi)}{d\xi^2}+\left(\frac{1-m^2}{4\xi^2}+\frac{\beta_1}{\xi}+\frac{\epsilon}{2}-\frac{F\xi}{4}\right)\chi^{\epsilon F}_{1n_1m}(\xi)=0, \tag{6}$$

$$\frac{d^2\chi^{\epsilon F}_{2n_1m}(\eta)}{d\eta^2}+\left(\frac{1-m^2}{4\eta^2}+\frac{\beta_2}{\eta}+\frac{\epsilon}{2}+\frac{F\eta}{4}\right)\chi^{\epsilon F}_{2n_1m}(\eta)=0, \tag{7}$$

where $\beta_1+\beta_2=1$. The ξ equation has a potential well, and thus presents a discrete eigenvalue problem. At any energy, the eigenvalues are the values of the separation constant β_1 for n_1 nodes in the ξ eigenfunction. Thus n_1 designates the different channels. The η equation in general has a barrier resulting from the combination of Coulomb field plus static field, and there is typically tunneling through this barrier. For $n_1>n$ ($\beta_1>1$, or $\beta_2<0$), the effective Coulombic potential in the η equation is repulsive and the wave function has small amplitude near the origin.

Near the origin, one can also write a wave function in spherical coordinates with quantum numbers l and m, and there is a transformation between the parabolic coordinate solutions and the spherical coordinate solutions:

$$\psi^{\epsilon F}_{n_1m}(\vec{r})=\frac{e^{im\phi}\chi^{\epsilon F}_{1n_1m}(\xi)\chi^{\epsilon F}_{2n_1m}(\eta)}{\sqrt{2\pi\xi\eta}}=\sum_l U^{\epsilon Fm}_{n_1l}\psi^{\epsilon}_{lm}(\vec{r}). \tag{8}$$

The lowest order coefficients and the normalization are defined as follows:

$$\chi^{\epsilon F}_{1n_1m}(\xi)\cong N_\xi\xi^{(m+1)/2}[1+\cdots], \quad \int_0^\infty d\xi'\,\chi^{\epsilon F}_{1n_1m}(\xi')/\xi'=1, \tag{9}$$

$$\chi^{\epsilon F}_{2n_1m}(\eta)\cong N_\eta\eta^{(m+1)/2}[1+\cdots],$$

$$\chi^{\epsilon F}_{2n_1m}(\eta)\overset{\eta\to\infty}{\to}\sqrt{\frac{2}{\pi k_2(\eta')}}\sin\left[\int^\eta k_2(\eta')d\eta'+\tilde{\theta}\right], \tag{10}$$

$$\psi^{\epsilon}_{lm}(\vec{r})\cong N_{\epsilon l}Y_{lm}(\theta,\phi)r^l[1+\cdots],$$

$$\int \psi^{\epsilon *}_{lm}\psi^{\epsilon'}_{l'm'}d\tau=\delta(\epsilon-\epsilon')\delta_{mm'}\delta_{ll'}. \tag{11}$$

In the above expressions, $k_2(\eta)=(-m^2/4\eta^2+\beta_2/\eta+\epsilon/2+F\eta/4)^{1/2}$ is the WKB wave number. The transformation matrix is then given by

$$U^{\epsilon Fm}_{n_1l}=a^{\epsilon m}_{n_1l}\frac{N_\xi N_\eta}{N_{\epsilon l}}, \quad a^{\epsilon m}_{n_1l}=\langle lm|j\mu_+j\mu_-\rangle. \tag{12}$$

The energy is $\epsilon=-1/(2\nu^2)$, $j=(\nu-1)/2$, and $\mu_\pm=[m\pm\nu(\beta_1-\beta_2)]/2$, where ν, j, and $\mu_\pm$ are in general not integral. For integer values, $a^{\epsilon Fm}_{n_1l}$ is a standard Clebsch-Gordan coefficient. For nonintegral values, it is obtained by substituting appropriate Γ functions in place of factorial expression in, for example, Edmonds's Eq. (3.6.11) [45]. Stark structure occurs in the N_η factor in $U^{\epsilon Fm}_{n_1l}$, so that at resonance values of the energy and field, N_η attains a local maximum.

The transformation matrices apply to the expression for the photoionization cross section:

$$\sigma^F=4\pi\alpha^2\hbar\omega\sum_{n_1,m,\tilde{m}}|\langle\psi^{\epsilon F}_{n_1m}|r_{\tilde{m}}|\psi_i\rangle|^2, \tag{13}$$

where ψ_i is the initial state wave function and $r_{\tilde{m}}$ is the dipole transition matrix element for polarization component $\tilde{m}$. In view of Eqs. (8) and (13), we can write

$$\sigma^F(\epsilon)=C\sum_{l,l',m,\tilde{m}}\langle\psi^{\epsilon}_{lm}|r_{\tilde{m}}|\psi_i\rangle\langle\psi_i|r_{\tilde{m}}|\psi^{\epsilon}_{l'm}\rangle\sum_{n_1}U^{\epsilon Fm}_{n_1l}\tilde{U}^{\epsilon Fm}_{l'n_1}$$
$$=C\sigma^0H^{\epsilon F}, \tag{14}$$

where $C=4\pi^2\alpha\hbar\omega$, and

$$\sigma^0_{l'l}(\epsilon)=\langle\psi^{\epsilon}_{lm}|r_{\tilde{m}}|\psi_i\rangle\langle\psi_i|r_{\tilde{m}}|\psi^{\epsilon}_{l'm}\rangle, \tag{15}$$

$$H^{\epsilon Fm}_{l'l}=\sum_{n_1}\tilde{U}^{\epsilon Fm}_{l'n_1}U^{\epsilon Fm}_{n_1l}. \tag{16}$$

$\sigma^0_{l'l}(\epsilon)$ is independent of field since ψ_i is localized near the origin and the integrands are significant only for $r\ll F^{-1/2}$. H^F contains the Stark structure.

This may also be written

$$\sigma^F(\epsilon)=C\sum_{l,l',m,\tilde{m}}\langle\psi_i|r_{\tilde{m}}|\psi^{\epsilon}_{l'm}\rangle[\langle\psi'|\psi\rangle^{-1}]^{\epsilon Fm}_{l'l}\langle\psi^{\epsilon}_{lm}|r_{\tilde{m}}|\psi_i\rangle \tag{17}$$

so that $H^{\epsilon Fm}_{l'l}=[\langle\psi|\psi\rangle^{-1}]^{\epsilon Fm}_{l'l}$ serves as a normalization factor.

For alkali-metal atoms, one replaces the hydrogenic spherical coordinate function $\psi^{\epsilon}_{lm}=f_{\epsilon lm}(\vec{r})=Y_{lm}(\theta,\phi)F_{\epsilon l}(r)/r$, where $F_{\epsilon l}(r)$ is a regular Coulomb function, by the phase-shifted function

$$\Psi^{\epsilon}_{lm}=\cos\delta_l f_{\epsilon lm}(\vec{r})-\sin\delta_l g_{\epsilon lm}(\vec{r}), \tag{18}$$

where $g_{\epsilon lm}(\vec{r})=Y_{lm}(\theta,\phi)G_{\epsilon l}(r)/r$, in which $G_{\epsilon l}(r)$ is the irregular Coulomb function [46]. The phase shift δ_l is simply related to the quantum defect through

$$\delta_l=\pi\mu_l . \tag{19}$$

To introduce a comparable phase shift into the parabolic functions, we consider the irregular η function, $\bar{\chi}^{\epsilon F}_{2n_1m}(\eta)$, which is shifted by $\pi/2$ in the well relative to $\chi^{\epsilon F}_{2n_1m}(\eta)$. Asymptotically, $\bar{\chi}^{\epsilon F}_{2n_1m}(\eta)$ and $\chi^{\epsilon F}_{2n_1m}(\eta)$ differ by a phase γ_{n_1}, but their amplitudes are identical. If $a<b<c$ are the classical turning points of the η equation, then for $a\ll\eta\ll b$

$$\chi^{\epsilon F}_{2n_1m}(\eta)=\frac{1}{R}\sqrt{\frac{2}{\pi k_2(\eta)}}\sin\left(\int_a^{\eta}k_2(\eta')d\eta'\right), \tag{20}$$

$$\bar{\chi}^{\epsilon F}_{2n_1m}(\eta)=\frac{1}{S}\sqrt{\frac{2}{\pi k_2(\eta)}}\cos\left(\int_a^{\eta}k_2(\eta')d\eta'\right), \tag{21}$$

and for $\eta\gg c$,

$$\chi^{\epsilon F}_{2n_1m}(\eta)\rightarrow\sqrt{\frac{2}{\pi k_2(\eta)}}\sin\left(\int_c^{\eta}k_2(\eta')d\eta'+\tilde{\theta}\right), \tag{22}$$

$$\bar{\chi}^{\epsilon F}_{2n_1m}(\eta)\rightarrow\sqrt{\frac{2}{\pi k_2(\eta)}}\sin\left(\int_c^{\eta}k_2(\eta')d\eta'+\tilde{\theta}+\gamma_{n_1}\right) \tag{23}$$

such that $W(\chi_2,\bar{\chi}_2)=\chi_2\bar{\chi}_2'-\chi_2'\bar{\chi}_2=-(2/\pi)\sin\gamma_{n_1}=-2/(\pi RS)$. From the WKB connection formulas using parabolic cylinder functions, $R^2=T^2\cos^2\Delta+T^{-2}\sin^2\Delta$, where T is the tunneling integral and Δ is the phase accumulated in the well plus a small correction for tunneling. (We omit indices n_1, m, ϵ, and F on R, S, T, and Δ.) The comparable expression for S^2 is obtained by the replacement $\Delta\rightarrow\Delta-\pi/2$: $S^2=T^2\sin^2\Delta+T^{-2}\cos^2\Delta$.

Harmin uses the equality of Green's function in spherical and in parabolic coordinates

$$G^c_m(r,r')=\pi\sum_l f^*_{\epsilon lm}(\vec{r})g_{\epsilon lm}(\vec{r}')$$

$$=2\sum_{n_1}\frac{\chi^{\epsilon F}_{1n_1m}(\xi)\chi^{\epsilon F}_{1n_1m}(\xi')\chi^{\epsilon F}_{2n_1m}(\eta)\bar{\chi}^{\epsilon F}_{2n_1m}(\eta')}{W(\chi^{\epsilon F}_{2n_1m},\bar{\chi}^{\epsilon F}_{2n_1m})} \tag{24}$$

to give

$$g_{\epsilon lm}(\vec{r})=\frac{e^{im\phi}}{\sqrt{2\pi}}\sum_{n_1}\chi^{\epsilon F}_{1n_1m}(\xi)\bar{\chi}^{\epsilon F}_{2n_1m}(\eta)U^{\epsilon Fm}_{n_1l}\csc\gamma_{n_1} \tag{25}$$

and thus

$$\Psi^{\epsilon F}_{lm}=(\cos\delta_l)\sum_{n_1}[(U^{\epsilon Fm})^{-1}]_{ln_1}\psi^{\epsilon F}_{n_1m}$$

$$-(\sin\delta_l)\sum_{n_1}\tilde{U}^{\epsilon Fm}_{ln_1}(\csc\gamma_{n_1})\bar{\psi}^{\epsilon F}_{n_1m} \tag{26}$$

$$=(\cos\delta)U^{-1}\psi-(\sin\delta)\tilde{U}(\csc\gamma)\bar{\psi}. \tag{27}$$

Note that the left side of Eq. (25) is phase shifted isotropically, while the right side is phase shifted on the negative z axis but not on the positive z axis ($\eta=0$). This deficiency "heals" quickly off the z axis, but may be a limiting factor in precision calculations.

The normalization factor for alkali-metal atoms is

$$\langle\Psi|\Psi'\rangle=[\cos\delta-(\sin\delta)\tilde{U}(\cot\gamma)U]U^{-1}\tilde{U}^{-1}$$

$$\times[\tilde{U}(\cot\gamma)U\sin\gamma-\cos\gamma] \tag{28}$$

$$=Q(H^F)^{-1}Q+(\sin\delta)H^F(\sin\delta)=(D^F)^{-1}, \tag{29}$$

where

$$Q=\cos\delta-(\sin\delta)h^F, \tag{30}$$

$$h^{\epsilon Fm}_{l'l}=\sum_{n_1}\tilde{U}^{\epsilon Fm}_{n_1l'}U^{\epsilon Fm}_{n_1l}\cot\gamma_{n_1}. \tag{31}$$

Below the saddle point, H^F is small except at a hydrogenic resonance, hence one may use the expansion

$$D^F=[1+(Q^{-1}H^F\sin\delta)^2]^{-1}Q^{-1}H^F\tilde{Q}^{-1} \tag{32}$$

$$=\frac{\tilde{q}H^Fq+\cdots}{|\det Q|^2+\mathrm{tr}[(\tilde{q}H^F\sin\delta)^2]+\cdots}, \tag{33}$$

where $\tilde{q}=Q^{-1}\det Q$ is the adjoint of Q. Hence resonances occur when

$$\det Q=\det[\cos\delta-(\sin\delta)h^F]=0. \tag{34}$$

Also, appreciable tunneling below the saddle point leads to a different representation. Since $N_\eta=B^{1/2}/R$, we can factor $U^{\epsilon Fm}_{n_1l}$ into a nonresonant part, $U^{\epsilon 0m}_{ln_1}=a^{\epsilon m}_{n_1l}N_\xi B^{1/2}/N_{\epsilon l}$, and the resonant part, R^{-1}. Furthermore, as $\sin\gamma=1/RS$, $\cot\gamma=\sin\Delta\cos\Delta[T^2-T^{-2}]$ and

$$h^{\epsilon Fm}_{l',l}=\sum\tilde{U}^{\epsilon 0m}_{l'n_1}U^{\epsilon 0m}_{n_1l}\frac{\cot\gamma_{n_1}}{R^2_{n_1}}$$

$$=\sum\tilde{U}^{\epsilon 0m}_{l'n_1}U^{\epsilon 0m}_{n_1l}\frac{\sin\Delta\cos\Delta[T^2-T^{-2}]}{T^2\cos^2\Delta+T^{-2}\sin^2\Delta}$$

$$\rightarrow\sum\tilde{U}^{\epsilon 0m}_{l'n_1}U^{\epsilon 0m}_{n_1l}\cot\Delta \tag{35}$$

when the tunneling integral T is large. In the final expression, T and γ do not occur.

The tunneling integral T and phase accumulated in the well, Δ, can be computed from WKB expressions. To check this approximation, we have computed these quantities by numerical integration using the Milne method as described by Alijah *et al.* [47]. Results from this numerical transcription of the FT method will be presented in Sec. VIII.

VI. *R*-MATRIX THEORY COUPLED WITH COMPLEX COORDINATE ROTATION

A. *R*-matrix theory for Rydberg states

Recent theoretical work combining R-matrix and complex coordinate techniques has provided a computational means of calculating Rydberg spectra of nonhydrogenic atoms in the presence of strong electric and/or magnetic fields with high precision [16–18,21].

We first summarize the fundamentals of R-matrix theory. Space is split into two regions separated by a spherical surface of radius a (typically several Bohr radii in size). For $0<r<a$ the dynamics is dominated by the complicated interactions among the nucleus and all the electrons. The external electric field is here very small compared to the intra-atomic electric field. To give an order of magnitude: in our experiments, the electric field is at most 10 kV/cm, as compared with the 50 MV/cm intra-atomic electric field seen by an electron at 10 Bohr radii from the nucleus. Hence, in this inner region, the effect of the external field can be neglected to lowest approximation. We will show in Sec. VI D how it may be taken into account perturbatively for very accurate calculations.

For $r>a$, the multielectronic character of the atom can be neglected. The Rydberg electron there is affected only by the Coulomb field of the ionic core and the external field. Since the characteristic excitation energy of the ionic core is several eV, which is much larger than the $\sim$meV energies characterizing the binding energies of the Rydberg states, the ionic core can be considered frozen and its effect on the Rydberg electron for $r>a$ represented by an effective potential. This potential is essentially Coulombic $-Z/r$ (with charge $Z=1$) but small corrections exist due to the core polarization, see Eq. (3). The quantum defect parameters express the accumulated phase shift at large r from the core itself and the core polarization potential. If the radius a is sufficiently large, core polarization effects may clearly be neglected for $r>a$. Thus in the outer region the Rydberg electron of the nonhydrogenic atom is described by the same Hamiltonian (not the same wave function) as the electron of a hydrogen atom.

By splitting space, we reduce the full problem to two simpler ones: a field-free atom for $r<a$, and a hydrogenic problem in the presence of the external field for $r>a$. Both are relatively easy to solve. The inner-region wave function can be obtained from a full multi-electron calculation or extracted from field-free spectroscopic results, as done in this paper. The outer problem can be solved numerically using, for example, diagonalization over a Sturmian basis. The difficulty (overcome by conventional R-matrix theory) lies in *matching* the solutions at $r=a$.

However, for Rydberg atoms where many energy levels have to be computed, this conventional theory requires the computation of many solutions for $r>a$, followed by a complicated search for roots. In Refs. [16,18], a more efficient technique has been presented. The idea is to solve *first* the inner problem, and then use its solution to build in directly information about $r<a$ on the boundary $r=a$ via a "Schneider term" [48] *before* solving the outer problem. This ensures that the solutions of the latter give automatically the energy levels of the full problem. The details in Refs. [16,18] can be summarized as follows. For $r\geqslant a$, the eigenfunction $\psi_\epsilon(\vec{r})$ with energy ϵ is expanded over reduced radial functions $R_l(r)$ for angular momentum l, multiplied by spherical harmonics $Y_{lm}(\theta,\phi)$:

$$\psi(\vec{r})=\sum_l \frac{R_l(r)}{r} Y_{lm}(\theta,\phi). \tag{36}$$

Substituting Eq. (36) in the Schrödinger equation with the additional Schneider boundary term yields

$$\sum_l \frac{1}{r}\left\{\frac{1}{2}\left[-\frac{d^2}{dr^2}+\frac{l(l+1)}{r^2}-\delta(r-a)\left(\frac{d}{dr}-B_l\right)\right]-\frac{1}{r}\right.$$

$$\left.+Fr\cos\theta-\epsilon\right\}R_l(r)Y_{lm}(\theta,\phi)=0, \quad a\leqslant r\leqslant\infty. \tag{37}$$

Away from the boundary $r=a$, Eq. (37) reduces to the Schrödinger equation for a hydrogen atom in a static electric field, as expected. However, Eq. (37) must incorporate a specific boundary condition at $r=a$ which depends on the B_l term. The term $\delta(r-a)d/dr$ in Eq. (37) makes the Hamiltonian Hermitian in the range $a\leqslant r<\infty$. In the Schneider method, the term B_l is determined by

$$B_l=\frac{1}{U_{\epsilon l}(a)}\left.\frac{dU_{\epsilon l}(r)}{dr}\right|_{r=a}, \tag{38}$$

where $U_{\epsilon l}(r)$ is the lth partial wave obtained from the inner region:

$$U_{\epsilon l}(r)=(\cos\delta_l)F_{\epsilon l}(r)-(\sin\delta_l)G_{\epsilon l}(r). \tag{39}$$

[$F_{\epsilon l}(r)$ and $G_{\epsilon l}(r)$ are regular and irregular Coulomb functions, respectively, as stated in connection with Eq. (18).] B_l depends on the energy and the structure of the ionic core through the quantum defects in $U_{\epsilon l}(r)$. References [16–18] demonstrate that, with such a choice, the eigensolutions of Eq. (37) give the energy levels and wave functions of the nonhydrogenic atom in the presence of the external electric field.

Solving this equation is not easy because the energy enters explicitly as one term of the equation and also via the energy dependence of the B_l. For Rydberg states and not too large a radius a, the energy dependence of the B_l is sufficiently slow to allow its value computed at some fixed energy to be used in determining, by numerical diagonalization of Eq. (37), several energy levels close to this. For highly accurate calculations, this approximation is not acceptable.

However, the experiments are performed at a fixed energy of the Rydberg state, scanning the electric-field value

through consecutive resonances. Since the B_l depend on energy, but not on electric-field strength, they need be computed only once and inserted into Eq. (37). We then expand the $R_l(r)$ in terms of a Sturmian basis:

$$S_{nl}^{(\xi)}(r)=\left[\frac{(n-l-1)!}{2(n+l)!}\right]^{1/2}(\xi r)^{l+1}\exp(-\xi r/2)L_{n-l-1}^{(2l+1)}(\xi r), \tag{40}$$

where $L_{n-l-1}^{(2l+1)}(\xi r)$ are associated Laguerre polynomials and ξ a free parameter. The expansion is

$$R_l(r)=\sum_n c_{nl}S_{nl}^{(\xi)}(r), \tag{41}$$

where the c_{nl} are coefficients to be determined.

Multiplying Eq. (37) by $S_{n'l}^{(\xi)}(r)Y_{lm}^*(\theta,\phi)$ and integrating over the solid angle $d\Omega$ and over the range $a<r<\infty$ yields the equations

$$\frac{1}{2}\sum_n \left\{\int_a^\infty S_{n'l}^{(\xi)}(r)\left[-\frac{d^2}{dr^2}+\frac{l(l+1)}{r^2}-\delta(r-a)\left(\frac{d}{dr}-B_l\right)\right]S_{nl}^{(\xi)}(r)dr\right\}c_{nl}-\sum_n\left\{\int_a^\infty S_{n'l}^{(\xi)}(r)\frac{1}{r}S_{nl}^{(\xi)}(r)dr+\epsilon\int_a^\infty S_{n'l}^{(\xi)}(r)\right.$$
$$\left.\times S_{nl}^{(\xi)}(r)dr\right\}c_{nl}=-2F\sum_n\left\{K_{ll-1}\int_a^\infty S_{n'l}^{(\xi)}(r)rS_{nl-1}^{(\xi)}(r)dr\right\}c_{nl-1}-2F\sum_n\left\{K_{ll+1}\int_a^\infty S_{n'l}^{(\xi)}(r)rS_{nl+1}^{(\xi)}(r)dr\right\}c_{nl+1}, \tag{42}$$

where $K_{ll'}=\int Y_{lm}^*\cos\theta Y_{l'm}d\Omega$ can be easily computed (see, for example, [49]).

These equations can be rewritten in matrix form as

$$\mathscr{A}\mathbf{x}=F.\mathscr{B}\mathbf{x}. \tag{43}$$

Hence, using this method, all the electric-field values where a Rydberg state exists with the prescribed energy are eigenvalues of a generalized eigenvalue problem. A single matrix diagonalization gives all the electric-field values where a peak is expected in the experimental spectrum.

The $\mathscr{A}$ and $\mathscr{B}$ matrices have a block structure due to the coupling of different l by the electric field. Since all radial integrals are taken over the range $a\leqslant r\leqslant\infty$, the diagonal properties of the Sturmian functions with n are lost. However, all the radial integrals can be evaluated analytically. In our calculations, the basis set is composed of all the Sturmian functions having n less than or equal to some maximum value $n_{\max}$. $\mathscr{A}$ and $\mathscr{B}$ are consequently banded symmetric matrices with dimension roughly $n_{\max}^2/2$. For solving the generalized eigenvalue problem (42), we use the Lanczos algorithm which allows the computation of a few dozen eigenvalues in a user-defined interval at relatively low cost [50].

B. Complex rotation

The method described in the preceding section is efficient below the saddle-point energy where Rydberg states are quasibound states. Above the saddle-point energy $\epsilon=-2\sqrt{F}$ (i.e., above the critical electric field $F=\epsilon^2/4$ at fixed energy), the diagonalization cannot converge to any sensible eigenvalue. There, the spectrum is composed of resonances, complex poles of the analytic continuation of the Green's function. The positions of these poles in the complex plane can be obtained using the method of complex rotation (also known as the complex coordinate method). This makes it possible to include *exactly* the effect of the atomic continua.

We define the complex Hamiltonian

$$H(\vartheta)=-\frac{e^{-2i\vartheta}}{2}\nabla^2-\frac{e^{-i\vartheta}}{r}+e^{i\vartheta}Fr\cos\theta, \tag{44}$$

where the following substitutions occur: $r\rightarrow re^{i\vartheta}$ and $p\rightarrow pe^{-i\vartheta}$. Note that this substitution of variables preserves the commutation relation between $\vec{r}$ and $\vec{p}$.

The power of this method lies in the fact that the spectrum of the complex operator $H(\vartheta)$ is composed of the bound states of $H=H(\vartheta=0)$ (if there are bound states; the corresponding eigenvalues are then purely real), of isolated complex eigenvalues which are the resonances of H and of continua (half lines rotated in the complex plane by the angle -2ϑ around their branch points). The corresponding eigenfunction is square integrable, which implies that it can be computed by numerical diagonalization in a basis such as Sturmians.

The combination of the complex coordinate method with R-matrix theory (with the Schneider method) has already been demonstrated for nonhydrogenic atoms in a strong magnetic field [16,18] and in parallel electric and magnetic fields [17]. This again involves splitting the space into two regions, solving separately the problem for the *rotated* Hamiltonian $H(\vartheta)$ in the two regions and matching the two solutions at $r=a$. Note that this has to be done for $H(\vartheta)$ as its eigenstates of interest are square integrable. It cannot be done directly for H itself as its resonance eigenfunctions are not square integrable functions and satisfy a different boundary condition at $r\rightarrow\infty$ [51]. From the mathematical point of view, it is equivalent to consider the unrotated Hamiltonian for complex coordinates and a complex boundary $r=ae^{i\vartheta}$ or the rotated Hamiltonian and a real boundary $r=a$. The latter is more natural and will be used throughout the paper.

For the specific case we are interested in, we want to solve the problem at fixed (real) energy of the electron. Using the same expansion of the wave function, Eqs. (36) and (41), but with complex coefficients c_{nl}, we obtain for the complex rotated problem a generalized eigenvalue problem very similar to Eq. (42):

$$\frac{e^{-2i\vartheta}}{2}\sum_n \left\{ \int_a^\infty S^{(\xi)}_{n'l}(r)\left[-\frac{d^2}{dr^2}+\frac{l(l+1)}{r^2}-\delta(r-a)\left(\frac{d}{dr}-B_l\right)\right] S^{(\xi)}_{nl}(r)dr \right\} c_{nl}$$
$$-\sum_n \left\{ \int_a^\infty S^{(\xi)}_{n'l}(r)\frac{e^{-i\vartheta}}{r}S^{(\xi)}_{nl}(r)dr+\epsilon\int_a^\infty S^{(\xi)}_{n'l}(r)S^{(\xi)}_{nl}(r)dr\right\} c_{nl}$$
$$=-2Fe^{i\vartheta}\sum_n \left\{ K_{ll-1}\int_a^\infty S^{(\xi)}_{n'l}(r)rS^{(\xi)}_{nl-1}(r)dr\right\} c_{nl-1}-2Fe^{i\vartheta}\sum_n \left\{ K_{ll+1}\int_a^\infty S^{(\xi)}_{n'l}(r)rS^{(\xi)}_{nl+1}(r)dr\right\} c_{nl+1}. \quad (45)$$

The structures of the $\mathscr{A}$ and $\mathscr{B}$ matrices are the same as for the unrotated problem. The various matrix elements are simply multiplied by various powers of $e^{i\vartheta}$ yielding complex symmetric matrices. The only complication is for the Schneider term itself which has to be estimated for the rotated problem. This requires the calculation of regular and irregular Coulomb functions for complex energy and complex radial coordinate as explained in Ref. [18]. The generalized complex symmetric banded eigenvalue problem is again numerically solved using the Lanczos algorithm.

The result is a set of complex values of the electric field F, the real part being the center of the resonance and -2 times its imaginary part being the width (in units of electric field) of the resonance when observed at fixed energy.

From the eigenvectors of the rotated problem, we can also extract the wave functions of the resonances [51], the excitation probabilities of the various resonances, and the photoionization cross section [18].

C. Implementation of the method

The calculations reported here have been carried out using the method described in the preceding section. We now describe the choice of parameters.

The first parameter is the matching radius a. It has to be chosen larger than the radius of the ionic core. Then in the vicinity of and beyond the boundary $r=a$, we can use a one-electron wave function. If, in addition, the electric-field term in the Hamiltonian can be neglected near $r=a$, i.e., $Fa^2 \ll 1$, then the one-electron wave function is a linear combination of regular and irregular Coulomb functions with coefficients depending only on the quantum defects at the energy of interest. The Schneider term is then determined from Eqs. (38) and (39) or the trivial extensions of these equations for complex boundary $ae^{i\vartheta}$.

Using a large radius a makes the outer calculation easier because the wave function has fewer oscillations and convergence is usually obtained with a smaller basis. However, too large a matching radius invalidates a basic hypothesis of the method, namely, the fact that the term Fz in the Hamiltonian can be neglected in the inner region. A good compromise is to use a matching radius between 5 and 20 Bohr radii. However, as explained in Sec. VI D, even this is too large for ppm accuracy.

The rotation angle is not a crucial parameter. Indeed, the resonances of interest are the narrow ones, which have very small imaginary parts. For example, below the saddle-point energy, most of the resonances have widths smaller than the numerical accuracy of the computer. The numerical results give widths of the order of 10^{-15} a.u., not significantly different from zero. Rotation angles as small as $\vartheta=0.01$ are sufficient there. Above the saddle point, the situation is different. There are many unconverged complex eigenvalues with large imaginary parts which fluctuate erratically as the basis size is increased. These broad resonances (originating from higher Rydberg states dominated by the external field) do not contribute significantly to the physics of the system. There are also converged complex eigenvalues, corresponding to the interesting resonances which usually lie close to the real axis (widths smaller than $10^{-10}-10^{-9}$ a.u.). For a sufficiently large basis, their positions are independent of the rotation angle (as long as it is large enough to "uncover" the resonance, typically $\vartheta>0.01$). It was found numerically that the large proliferation of broad resonances spoils the convergence of the complex coordinate diagonalization. This is not really surprising [51] and is probably due to a weak instability of the Lanczos algorithm for complex symmetric matrices. To overcome this problem, we used small rotation angles (0.01) and wrote a specific version of the Lanczos algorithm using partial pivoting [52].

The choice of the scaling parameter ξ of the Sturmian basis, Eq. (40), is also important. Too large a value requires a very large basis while too small a value prevents the numerically computed wave function from reproducing correctly the oscillations of the exact wave function near the boundary, thus destroying completely the convergence. For the parameter value $\xi=2/n$, the Sturmian function $S_{nl}(r)$ coincides with the radial wave function of the hydrogenic Rydberg state with principal quantum number n. Thus it is natural to use, at a fixed energy ϵ, the value $\xi=2/n^*=2\sqrt{-2\epsilon}$ corresponding to nearby Rydberg states ($n^*\simeq 15$ for the results reported here). We observed that a slightly lower value of ξ gave much better results (faster convergence) at the price of a small increase in basis size. With the optimal choice of the parameter ξ, good convergence in the region of interest (principal quantum number about 15) is obtained using a Sturmian basis with $n_{\max}=40-50$ below the saddle point and $n_{\max}=60-70$ above. The corresponding size of the basis ranges from 800 to 2500. All the calculations reported here have been performed on an ordinary Sun workstation. The CPU time was always short, never exceeding 5 min to get all the resonances of interest at a fixed value of the energy.

Finally, there was a problem with the large-l components of the wave function. Although they have very small quantum defects, they can strongly affect the convergence of the calculations, especially above the saddle point. The reason for this is that in our R-matrix method, we assume that the

atomic potential is purely Coulombic outside the matching radius, which makes it possible to use the regular and irregular Coulomb functions with coefficients corresponding to the phase shift originating inside the matching radius. This is not true for high-l values, where the quantum defect is not due to core penetration, but to core polarization or to the relativistic mass correction, either of which are associated with a long-range potential. This means that most of the phase shift at infinity is actually accumulated not inside but outside $r=a$. Hence, at $r=a$, although the physical reduced radial function is very small, going smoothly to zero as r^{l+1}, the function used in the calculation containing a nonzero quantum defect does not have these characteristics. In fact, the irregular Coulomb function, even though its coefficient is very small, makes a much bigger contribution than the regular one, and leads to a wrong estimation of B_l. To overcome this problem, one can increase the matching radius—which pushes the problems to higher-l values—and further set the quantum defects of high-l values exactly to zero. Doing this, we neglect the quantum defects of states with l larger than 7 or 8 (see Sec. VIII). Keeping all the quantum defects nonzero usually gives results that are not very well converged, especially above the saddle point.

D. Improving the accuracy of the results

Since we are trying to obtain results that are as accurate as possible, we now consider possible causes for errors and inaccuracies. The complex rotation method takes all the couplings with the continuum and between continua exactly into account. The basis size is not a serious limitation, as it can be easily extended—even on a workstation—to get fully converged results. Hence, neglecting the core polarization potential beyond $r=a$ (which is fully justified if a is large enough), we are able to solve the problem in the outer region with an accuracy limited only by the numerical rounding errors. Taking into account the weak instability of the Lanczos algorithm, we estimate the eigenvalues obtained by solving the outer problem to be accurate to ten significant figures, which is not a serious limitation.

The main difficulty comes in fact from the *inner* region. The first limitation concerns knowledge of the quantum defects, which is discussed in Secs. III B and VIII. A more fundamental limitation comes from the assumption that we can neglect the effect of the electric field for $r<a$ and thus use pure Coulomb functions to determine the boundary condition at $r=a$. The order of magnitude of the error made using this assumption can be estimated from Eq. (37). The term in this equation that couples the various l channels is $Fr\cos\theta$. For l mixing to be negligible, for $r<a$ this term has to be much smaller than the Coulomb potential (diagonal in l) at $r=a$. Hence the condition for neglecting the l mixing in the inner region is

$$Fa \ll \frac{1}{a}. \tag{46}$$

However, for a typical situation of interest, we have $F\simeq 10^{-6}$ a.u.$\simeq 5$ kV/cm and $a\simeq 10$ a.u., which means that the l-mixing term can be as large as 10^{-4} relative to the diagonal term. Hence we can expect in the real system a mixing between computed states of the order of 10^{-4}. The electric field strongly mixes the various l channels in the outer region and the effect of the l mixing in the inner region can consequently induce errors in the determination of the energy levels (at fixed electric field) or in the determination of the electric-field values (at fixed energy) in the fourth or fifth digit. This is clearly not acceptable for measurements at our present level of precision.

To solve this problem, we remark that the same strategy (i.e., solving the problem for $r>a$ by diagonalization) can be kept provided we are able to insert at the boundary $r=a$ the correct physical Schneider term associated with the exact solution in the inner region. Because of the l mixing for $r<a$, the Schneider term will lose its diagonal character. In other words, a solution in the inner region which is a pure l wave close to the nucleus will progressively evolve into a linear combination of several l waves as it propagates outwards. We need to know what the wave will actually be at radius $r=a$. Fortunately, the electric-field-induced mixing in the inner region is small and can be treated perturbatively [higher order terms will be at most of the order of $(10^{-4})^2$, and hence do not have to be considered here]. In the inner region, as soon as the electron leaves the ionic core, it is affected by the superposition of the Coulomb plus external field potential. Hence, if we expand the wave function as in Eq. (37), the following equation has to be satisfied between a small radius $r=b$, slightly outside the ionic core, and the boundary $r=a$:

$$\sum_l \frac{1}{r}\left\{\frac{1}{2}\left[-\frac{d^2}{dr^2}+\frac{l(l+1)}{r^2}\right]-\frac{1}{r}+Fr\cos\theta-\epsilon\right\} \times R_l(r)Y_{lm}(\theta,\phi)=0. \tag{47}$$

Hence we are faced with the problem of propagating an initially pure l wave from $r=b$ to $r=a$. This is a well known problem which can be solved using an R-matrix approach once again.

Because of the selection rules on the angular variables, $\Delta l=\pm 1$, only channels $l-1$, l, and $l+1$ will be mixed to first order. *A priori*, any complete set of solutions of Eq. (47) can be used to propagate from the ionic core to $r=a$. It is particularly convenient to consider as base solutions those which are pure l waves at the boundary. Let us consider a basis of such solutions $\psi^{[l]}(\vec{r})$ whose spherical components will be denoted $R_{l'}^{[l]}(r)$. They are chosen such that

$$R_{l'}^{[l]}(a)=\delta_{ll'}U_{\epsilon l}(a). \tag{48}$$

With this constraint, it is of course in general not possible to choose simultaneously $(dR_{l'}^{[l]}/dr)(r=a)=0$, which is possible only in the absence of l mixing. Hence the nonzero derivatives will give nondiagonal contributions to the Schneider term. These can be easily computed to first order in the electric field F by multiplying Eq. (47) for $\psi^{[l]}(\vec{r})$ by the Coulomb function $U_{\epsilon l+1}(r)$ and integrating between the small radius b and the boundary a. To first order, the function $R_l^{[l]}(r)$ will be the main contribution while the other $R_{l'}^{[l]}(r)$ will be $O(F)$ times smaller. Also, to the same order, $R_l^{[l]}(r)$ has to coincide with $U_{\epsilon l}(r)$. Hence one obtains

$$B_{l+1,l}=\frac{1}{R_l^{[l]}(a)}\left.\frac{dR_{l+1}^{[l]}}{dr}\right|_{r=a}$$
$$=FK_{ll+1}\frac{\int_b^a U_{\epsilon l}(r)U_{\epsilon l+1}(r)rdr}{U_{\epsilon l}(a)U_{\epsilon l+1}(a)}. \quad (49)$$

$B_{l+1,l}$ defines the nondiagonal Schneider term which has to be included between blocks l and $l+1$. More precisely, one obtains a generalized eigenvalue problem similar to Eq. (42) with the simple additional term

$$\frac{1}{2}\sum_n B_{l+1,l}S^{(\xi)}_{n'l+1}(a)S^{(\xi)}_{nl}(a)c_{nl} \quad (50)$$

in the left side of the equation.

Thus, to first order, the nondiagonal Schneider term preserves the selection rule $\Delta l=\pm 1$, and consequently the banded structure of the matrix. Also, from Eq. (49), the symmetric character of the $\mathscr{H}$ matrix is preserved. The physical interpretation of Eq. (49) is simple: the integral represents the matrix element of the dipole operator between unperturbed Coulomb functions, taken in the inner region. Since $B_{l+1,l}$ represents a small correction, it is appropriate to neglect the effect of $U_{\rm pol}$ [see Eq. (3)] on the wave functions $U_{\epsilon l}(r)$ for $b<r\leqslant a$. The choice of the lower bound b for the integration has to be made from physical arguments: b must be larger than the radius of the ionic core, so that the $U_{\epsilon l}(r)$ functions are solutions of the physical problem. In our calculations, we used $b=1$ or 1.5 Bohr radii, without observing significant differences. At such a distance, the l mixing induced by the electric field is actually negligible. Its order of magnitude can be obtained from the polarizability of the ionic core by a static electric field. With an R-matrix approach, there is no hope to go beyond this limit. Indeed, the polarizability of the core depends on the complicated multielectron interaction. In the present case of Li, it can be roughly estimated to be of the order of 10^{-10} a.u. of energy at 10 kV/cm. This might cause errors of the order of a small fraction of a ppm in the calculation of the resonance positions at large fields.

Finally, the importance of the nondiagonal Schneider term in obtaining highly accurate results is illustrated in Fig. 5, which shows the computed position of a typical resonance (real part) as a function of the boundary radius a with and without the nondiagonal Schneider term, all other parameters being kept fixed. At small a, the calculations do not converge well. In the range 7–20 Bohr radii, the computation without the nondiagonal Schneider term oscillates—which demonstrates that l mixing is not small in such inner regions—while the full computation is perfectly converged, with an accuracy much better than 1 ppm.

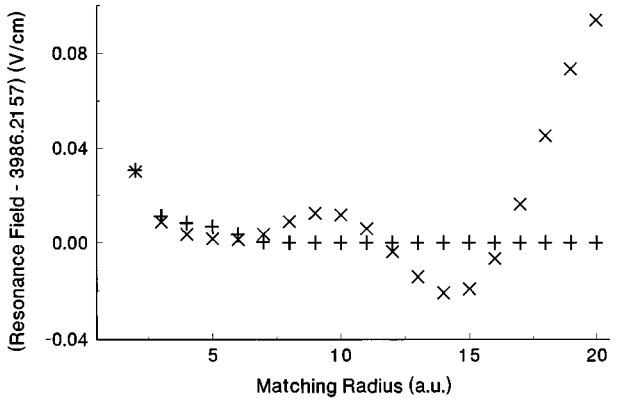

FIG. 5. A typical result showing the influence of field-induced l mixing in the inner region for an R-matrix calculation. The figure displays the position of a resonance as a function of the matching radius used in the calculation (the basis has a fixed size of 1800). The crosses ($\times$) are obtained for a simple calculation without l mixing in the inner region: the accuracy is limited to a few ppm. In contrast, when the l mixing is taken into account ($+$) by a nondiagonal Schneider term, a far better accuracy is obtained.

VII. INTERFERENCE NARROWING MEASUREMENTS

Resonance narrowing occurs when two or more broad energy levels interact in such a way that the couplings with continuum channels interfere, decreasing the decay rate by possibly several orders of magnitude over a small range of field. Although our experiment in Li was designed to measure resonance positions rather than lifetimes, we are able to measure resonance widths and thus to study interference narrowing. Of course, our width measurements were limited by instrumental factors, such as field inhomogeneity, laser width, and transverse Doppler width. We studied three separate narrowing regions to evaluate the feasibility of using these features for field calibration with our existing setup. Only one of the narrowings we examined was found to be useful for calibration given our experimental resolution. In the other cases, the calculated deep minimum width was masked by the experimental width so that only a broad, flat minimum was observed. Since the voltage offset must be fit in addition to the effective electrode separation, the range of voltages over a single narrowing region does not provide a precise fit to these two parameters. The data we obtained for the ''best'' narrowing recorded does, however, show excellent agreement with RM calculations and is presented here as an additional comparison with the RM and FT theories.

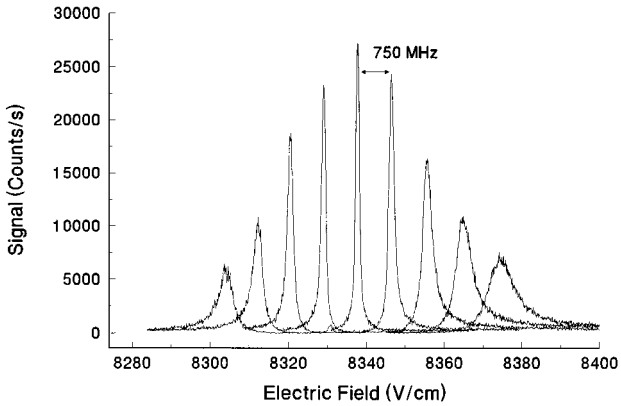

FIG. 6. Line shapes observed from successive electric field scans shown with energies differing by 750 MHz (twice the reference cavity mode separation), illustrating interference line narrowing. The central peak has energy of $-482.898\,25(4)\ \mathrm{cm}^{-1}$ calibrated using MD in conjunction with low-field resonance data. The x axis has likewise been calibrated in units of field, using the same low-field data. The resonances near the minimum width are nearly symmetric.

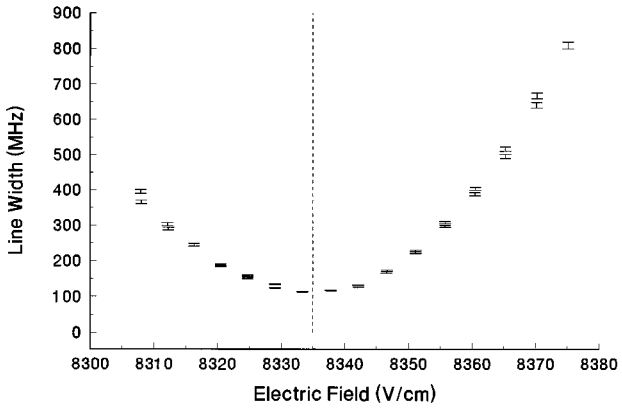

FIG. 7. Linewidths determined from the data shown in Fig. 6. The fitted minimum occurs at 8334.96(12) V/cm.

Figure 6 shows the general appearance of a region of interference narrowing. Each individual peak represents a field scan at a fixed excitation frequency from the Li $3\,^2S$ level. The laser frequency of the final step to Rydberg levels is adjusted between each peak measurement and locked to a stabilized Fabry-Pérot reference cavity. The recorded resonance data sets are separated by the cavity's free spectral range, 375(1) MHz (those shown in the figure are separated by twice this, 750 MHz, to make the figure intelligible). Near the minimum width, the line shapes are roughly symmetric, but away from the minimum, asymmetric Fano shapes appear. We extracted values for the linewidths by fitting Gaussian line profiles to the symmetric resonances. The widths are plotted as a function of field in Fig. 7. These points were fit with a quadratic function of field near the minimum in order to obtain an optimum value for the voltage at which the narrowing reaches a minimum.

To compare with theory, we calibrated the field by measuring seven resonance peaks at low field, using the method outlined below. These data yielded an effective plate separation of 0.720 862 0(27) cm, zero-field offset of $-0.1197(57)$ V, and an energy of $-482.898\,25(4)\ \mathrm{cm}^{-1}$. Using these parameters, the field at the minimum width was found to be 8334.96(12) V/cm (14 ppm uncertainty). RM calculations predict the value to be 8334.93 V/cm, well within our experimental uncertainty. By contrast, FT calculations predict the narrowing minimum to occur at 8336.57(06) V/cm, giving a discrepancy of more than 190 ppm.

VIII. COMPARISON BETWEEN THEORY AND EXPERIMENT

The primary goal of the present work was to demonstrate a precision (ppm level) calibration of the electric field, by comparing measurements of Li Stark resonance voltages with theory. For reasons discussed below, all final data fits have been made with results from *R*-matrix theory. The deficiencies of MD and FT methods will then be made evident. Our data thus offer insights into the ultimate limitations of these two approaches, and a confirmation of the higher accuracy achievable with the RM method.

The fitting procedure also provides a value for the atomic binding energy of the upper level of the laser transition. In work on Na [2], such information has been used together with an accurate value for the laser frequency to provide improved information on the binding energy of the lower level. In the present case, this would be the Li $3\,^2S$ state, but in our experiments, the absolute laser frequency was not accurately known. However, a discussion of the error limits for the energy determination as well as for the field calibration is of interest with regard to the future possibilities for the determination of the binding energy of the Li $3\,^2S$ state. We will discuss effects caused by the Stark shift of the $3\,^2S$ level, uncertainties in the quantum defect parameters, the polarization potential, and relativistic terms in the Hamiltonian used to compute the Stark wave functions.

The fits to our ''best'' data sets were significantly improved by including the Stark shift of the $3\,^2S$ state. Values for this shift were obtained by MD and RM calculations and found to agree to within 0.2% of the value from the $3\,^2S$ polarizability of 1.103×10^{-11} a.u. calculated by Themelis and Nicolaides [53]. The shift is very nearly quadratic and equal to 51.4 MHz at 10 kV/cm. It is important in the following discussion that the 813-nm laser was always locked to the $2\,^2P\rightarrow3\,^2S$ transition in the *field-free* fluorescence region (see Fig. 2 and Sec. II). One of us (C.H.I.) has carried out a calculation for two-photon excitation in a three-level system. We find that the importance of a shift of the intermediate state depends on the linewidth of the two lasers. In the case of extremely narrow lasers and atomic linewidth, the spectrum of a two-photon transition will depend only on the initial and final states, and will not be affected by a shift of the intermediate state. On the other extreme, if the laser has a wide frequency bandwidth or the intermediate state is sufficiently broadened by radiative decay or by Doppler effects, the intermediate state can be excited by the wings of the first laser, and the two-photon spectrum will depend on the position of the intermediate state. (A related calculation has been carried out in Ref. [54].) For our estimated experimental conditions with relatively broad laser linewidth, the results of our model are consistent with the conclusion that the Stark shift of the $3\,^2S$ state should be included. For certain scans, the 813-nm laser was narrow enough to produce an intermediate situation in which the $3\,^2S$ Stark shift was only partly evident, hence fits either with or without the $3\,^2S$ Stark shift gave results of poorer quality than with data obtained with a broader laser.

To obtain a field calibration, the voltage scan data were fit to Gaussian resonance shapes to extract resonance voltages, as shown in Fig. 4, and then the resonance voltages were fit to calculated resonance positions. Initially, fitted peak positions below the saddle point were fit to energy levels calculated by MD theory, using polynomials fitted over a series of (energy)/(field) values for the various Stark components. The energy, calibration factor (effective electrode spacing), and voltage offset were adjusted to achieve the best least squares fit to the resonance peak positions. To minimize the correlation between the fitted field and energy parameters, it is essential that the measured resonances exhibit different slopes, preferably of opposite sign. For this reason, the ''spaghetti'' region of many avoided crossings is especially useful. Eventually, RM results became available, and could be extended beyond the saddle point. The extracted parameters obtained with MD and RM methods diverged, and for reasons dis-

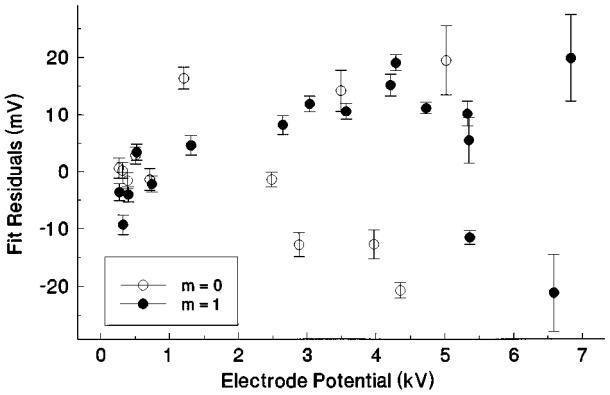

FIG. 8. Residuals (calculated minus observed values) from a fit of measurements of 27 peaks to RM calculations, using QD parameter set A and μ_l as given in Table III for $4 \leqslant l \leqslant 7$. The $m = 0$ (open circles) and $|m| = 1$ (closed circles) data were fitted together. The calibration parameters obtained from the fit are $d_0 = 0.723\,716\,7(10)$ cm, offset voltage $V_o = 0.2630(31)$ V, and $E_0 = -483.060\,897(24)$ cm^{-1}.

cussed below, it became evident that MD results were inaccurate at the level of precision attained experimentally.

Figure 8 shows a plot of residuals from a least squares fit of resonance positions to RM results obtained with 2450 basis states (results with 1800 basis states differed only slightly). Most peaks are fit to better than 15 mV (20 mV/cm). The residuals are three to ten times larger than the uncertainties from the fits to the individual peak positions (shown as error bars in Fig. 8). There was possibly a small drift of the high voltage dc power supply while the individual peaks were scanned (the voltage was recorded before and after scanning each peak), or small drifts of the laser frequency during or between the peak scans. This suggests that improved stabilization of the power supply and lasers might lead to several times better precision.

Figures 9 and 10 show the error limits for the electrode spacing and energy parameters. The first data point in each figure shows the result with all 27 narrow resonances ($m = 0$ and $|m| = 1$ peaks together) with the quantum defect parameter set A given in Table II for $l \leqslant 3$, with the QD parameters given in Table III for $4 \leqslant l \leqslant 7$, and with all $\mu_l = 0$ for $l > 8$. Results of a fit with μ_7 also set to zero are shown in the second line. The third line of Figs. 9 and 10 gives results with QD parameter set B (Table II), and μ_7 again as in Table III. Since the interpolated energies for the 15 ^2D and ^2F states differ by about 9 and 7 MHz, respectively, between QD fit A and fit B (as indicated in Table II), the value of the fitted energy changes by about 1 MHz, and the fitted value for d changes by just 0.5 ppm. This provides one indication of the effect of uncertainties in the QD parameters on the fit results. Another indication is provided by the changes of the results when QD parameters are varied by the standard deviations obtained from fits A and B. These changes were smaller than the differences between results with QD set A and B.

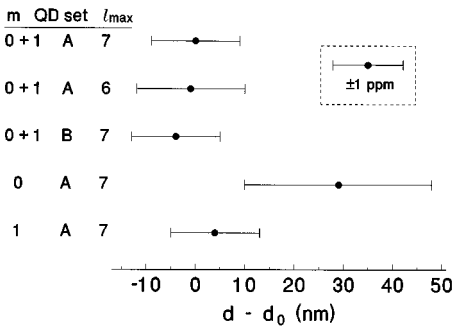

FIG. 9. Fitted values of the effective electrode plate separation d from comparisons of the experimental peaks with RM calculations. The value d_0 is given in the caption for Fig. 8. The top two lines give the results of fits of $m = 0$ and 1 peaks with QD parameter set A, the third line with QD parameter set B, the fourth line gives results with a fit of $m = 0$ peaks only, and the fifth line gives results with $|m| = 1$ peaks only. In each case, μ_l values are as given in Tables II and III, (and $\mu_l = 0$ for $l \geqslant 8$) except for the second line, for which $\mu_7 = 0$.

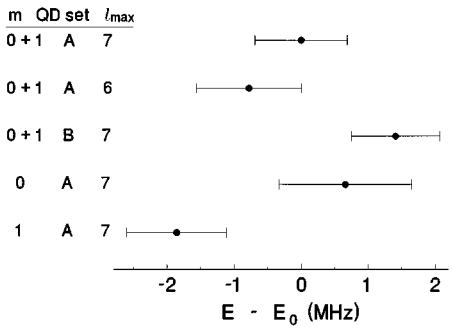

FIG. 10. Fitted values of the binding energy of the upper level of the laser-excited transition from comparisons of experimental peak positions and RM calculations. The various fit results are labeled as in Fig. 9. E_0 is given in the caption for Fig. 8.

The fourth and fifth lines in Figs. 9 and 10 show results of a fit with just the $m = 0$ and $|m| = 1$ peaks, respectively. The results for the electrode spacing d differ by almost 4 ppm, but the error limits overlap. Because E is also fitted, the fitted value for d from the fits with $m = 0$ and $|m| = 1$ peaks separately are both greater than from the combined fit. For the fitted value of E, the $|m| = 1$ peaks alone gave a result less than the combined fit by slightly more than the combined error limits.

The R-matrix method cannot easily accommodate the small quantum defect parameters for $l \geqslant 8$ that arise from the relativistic mass correction term $E_{\rm rel}$ and the polarization potential. These phase shifts accumulate primarily in the region $r > a$. The average energy shift from these omitted quantum defect parameters is mostly cancelled (to ≈ 1 MHz) by the positive energy shifts from the n^{-4} part of $E_{\rm rel}$, which are not included in the QD-shifted energies. In view of the correlation between the fitted E and d parameters, we estimate that the net effect of the omitted quantum defect parameters and the omitted n^{-4} terms from $E_{\rm rel}$ on d is approximately 0.3 ppm.

After the additional uncertainties in the field calibration due to uncertainties in the fitted QD parameters and due to neglecting high-l QD parameters is taken into account, we believe the calibration parameter (d) is accurate to $\pm$ 2 ppm, and the fitted energy is accurate to 1.5 MHz.

Direct comparisons of calculated resonance energies below the saddle point obtained from RM and MD methods show that the *ad hoc* extrapolation procedure discussed in

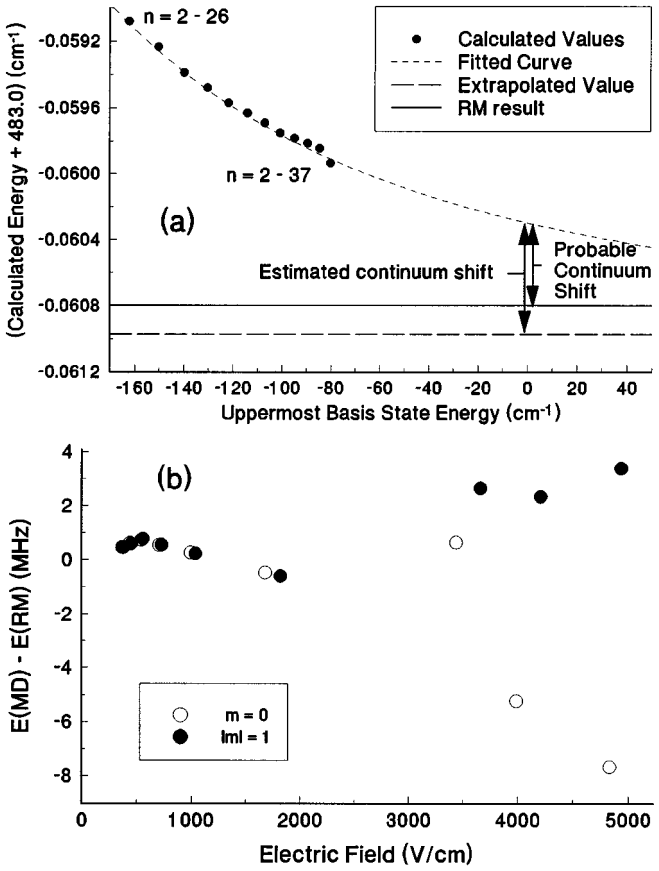

FIG. 11. An evaluation of MD results. (a) A plot of fits to MD eigenvalues, $E(E_{\max})$, as a function of the energy $E_{\max}$ of the uppermost level in the basis set. The fitting function is Eq. (5) in the text. The fitted energy E_∞ (dashed line) includes an estimate for the shift from coupling with continuum levels. However, E_∞ is about 6 MHz below the RM result (solid line) for this resonance. (b) Open and closed circles show differences between E_∞ values from MD calculations and RM results for 18 Li resonances at -483.0609 cm^{-1}.

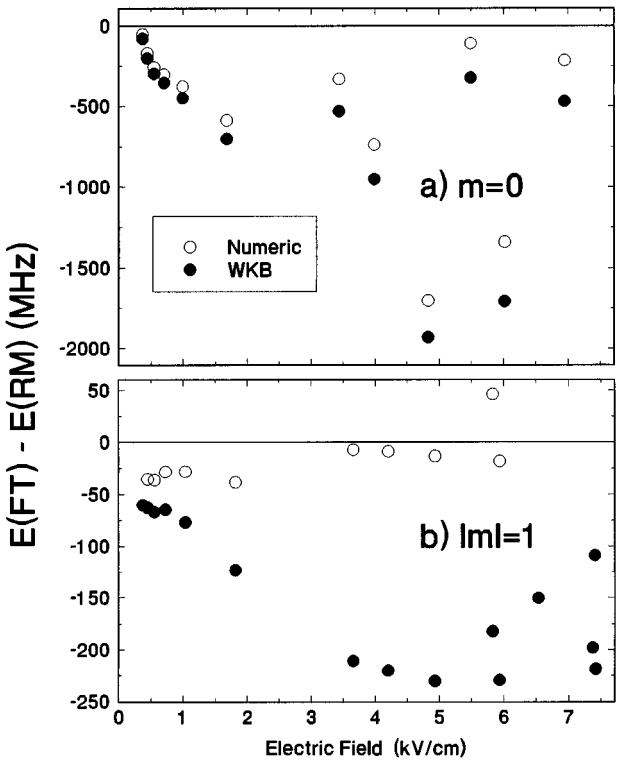

FIG. 12. Deviations between FT results and RM results for the observed peaks. Filled circles refer to WKB results, open circles refer to results obtained with numeric wave functions. (a) $m=0$ peaks; (b) $|m|=1$ peaks.

Sec. IV [Eq. (5)] can yield estimated energies within a few MHz of the RM values. Figure 11(a) shows a series of eigenvalues for the $m=0$ resonance at 4831 V/cm and $E=-483.0609$ cm^{-1} calculated with basis states from $n=2$ up to various n values as indicated. Extraneous weakly coupled nearby eigenvalues from drastically shifted high-n levels produce small deviations of the data points from a smooth curve. Because of these effects and the approximations in this procedure, the extrapolated value for E_∞ does not agree exactly with the RM value, shown as the horizontal solid line in Fig. 11(a). Figure 11(b) shows differences between the extrapolated MD results and RM results for each observed resonance below the saddle point at a binding energy of -483.0609 cm^{-1}. As discussed in Sec. IV, the value for the exponent β was chosen from a comparison between MD results and "exact" results for hydrogen $n=15$ $|m|=1$ levels. The close agreement with RM results for Li using this procedure corroborates RM results to the level of a few MHz, although their accuracy is believed to be considerably better. This comparison also suggests that if RM results are not available, extrapolation of MD results as a function of $E_{\max}$ offers an alternative procedure of moderately high accuracy provided one stays sufficiently far below the saddle point.

Taking the field calibration and energy parameters from the RM fit, we find that calculations with the FT approach differ by relatively large amounts. Figure 12(b) shows that for $|m|=1$ peak positions, FT theory with WKB wave functions was within 250 ppm, and was significantly better when numeric wave functions rather than WKB approximations were used. However, deviations for $m=0$ peaks shown in Fig. 12(a) were as much as 2 GHz, and only marginally improved by the use of numeric wave functions (open circles in Fig. 12). The energy shifts relative to RM results shown in Fig. 12 for $|m|=1$ peaks translate into shifts of the resonance voltages of typically 150 ppm for WKB wave functions and 25 ppm for numeric wave functions. The $m=0$ resonance energy shifts correspond to 1000–5000 ppm shifts in field, with the numeric wave function FT results about 10% closer to RM values than the WKB FT results.

One potential source of error that may account for the large residuals with the FT approach is Eq. (25). Numerical calculations of the sum in this equation confirm that the phase shift from the right hand side is not isotropic. We are investigating an alternative approach in which phase-shifted functions of ξ as well as of η are used. This entails a fundamentally different approach [55].

IX. CONCLUSIONS

We have demonstrated a calibration of the applied electric field to about ± 2 ppm ± 4 mV/cm by comparing observed

Stark resonances in ^{7}Li with calculated resonance positions. The error limits correspond to the uncertainty in the fitted electrode spacing and in the fitted voltage offset parameter. The optimum experimental technique was found to be a scan of resonances as a function of voltage with frequency-stabilized lasers. The optimum theoretical approach was found to be the R-matrix method with complex rotation, using a basis of Sturmian functions. This method agreed well with experimental results both below and above the saddle point. Empirical quantum defect parameters for Li, required in this calculation, were fitted from available zero-field spectral data. Uncertainties in the QD expansion parameters affect the field calibration by about 0.3 ppm.

The matrix diagonalization approach could be used only below the saddle point and its accuracy suffered because only discrete states could be included in the basis. An extrapolation technique used to estimate the continuum contributions resulted in somewhat better agreement with R-matrix results.

Although FT theory is attractive and reliable at lower precision, it gives results (with WKB wave functions) that deviate from experiment by up to thousands of ppm for $m=0$ resonances, although $|m|=1$ resonances are in every case within 200 ppm. When numerical wave functions are substituted for WKB wave functions, there is relatively small improvement for the $m=0$ resonances, but typically the $|m|=1$ peaks move to within 50 ppm of RM values. This behavior is not fully understood. We have noted that the phase shifts in FT theory are not isotropic near the origin and this may affect the accuracy of the results, but it is not clear why the $|m|=1$ peaks should be more accurate and also more significantly improved with numeric wave functions than the $m=0$ results.

The data suggest the presence of drifts in the power supply voltage and/or the laser frequencies. A more stable high voltage supply and additional laser frequency stabilization might improve the quality of the calibration by an order of magnitude. Also, we note that the energy of the upper state is fitted to approximately 1.5 MHz, suggesting that this technique, when combined with accurate knowledge of the laser frequency, might be used to determine the binding energy of the lower state of the last transition to this level of precision.

We have also presented measurements of interference line narrowing showing good agreement with RM calculations, using a field calibration from resonance measurements at low field. With cw lasers, line narrowing measurements themselves do not give as precise a field calibration as the measurements of line positions. However, these measurements do demonstrate the successful application of RM theory to linewidth measurements.

ACKNOWLEDGMENTS

We thank Mihai Negoescu, Stefan Haaf, and Sandra Williams for technical support and R. Drachman, A. Bhatia, and G. Drake for helpful conversations about the polarization model and quantum defect expansions. We are indebted to Professor L. Radziemski for communicating spectral data prior to publication. The work at Stony Brook is sponsored by the National Science Foundation. A grant of computer time from the Cornell Theory Center made the MD calculations possible. Laboratoire Kastler-Brossel, de l'ENS et de l'UPMC, is unité associée 18 du CNRS. The RM computational effort was supported in part by the UK Engineering and Physical Sciences Research Council and by the Alliance British French Research Programme. I.S. acknowledges support by the German Academic Exchange Service (DAAD - HSP II program) and the Deutsche Forschungsgemeinschaft.

APPENDIX: UNITS OF ENERGY AND ELECTRIC FIELD

To translate our theoretical results into laboratory units, precise values of the atomic units of energy and field are needed. These are obtained from the fundamental constants as described below.

For measurements on Rydberg states, it is appropriate to consider neutral Li to be a one-electron atom whose "nucleus" has the mass of the Li^+ ion core, $M=M_A-m$, where M_A is the atomic mass and m the electron mass. (This ignores the contribution to M_A from the binding energy of the outer electron, which is of the order of 10^{-8} amu.) The reduced mass is then $\mu=mM/(M+m)$. After separating out the center-of-mass motion, the Schrödinger equation for the outer electron is [in Système International (SI) units to facilitate comparisons with tables of the fundamental constants]

$$\left[\frac{-\hbar^2}{2\mu}\nabla_\rho^2-\frac{Ze^2}{4\pi\epsilon_0\rho}-V_{\rm pol}(\rho)-F_{\rm SI}e\zeta\right]\Psi=E_{\rm SI}\Psi, \tag{A1}$$

where $Z=1$ here, $V_{\rm pol}(\rho)$ is a potential associated with the polarization of the core (see Sec. III), $F_{\rm SI}$ is the applied external electric field in SI units, and $E_{\rm SI}$ is the energy in SI units. To translate to atomic units, we write $\rho=ar$ and $\zeta=az$, where a is a scaling parameter (the Bohr radius). We obtain

$$\left[\nabla_r^2+\frac{2\mu a^2}{\hbar^2}\left(\frac{Ze^2}{4\pi\epsilon_0 ar}+V_{\rm pol}(ar)+F_{\rm SI}eaz+E_{\rm SI}\right)\right]\Psi=0. \tag{A2}$$

This assumes the simple form

$$\left[\nabla_r^2+2\left(\frac{Z}{r}+U_{\rm pol}(r)+Fz+\epsilon\right)\right]\Psi=0 \tag{A3}$$

after appropriate substitutions are made. In particular,

$$a=\frac{4\pi\epsilon_0\hbar^2}{\mu e^2}=\left(\frac{m}{\mu}\right)\frac{\alpha}{4\pi R_\infty}=\left(\frac{m}{\mu}\right)a_\infty. \tag{A4}$$

In Eq. (A4), we have used the definitions in SI units:

$$\epsilon_0=\frac{1}{\mu_0 c^2},\quad \alpha=\frac{\mu_0 ce^2}{2h},\quad R_\infty=\frac{mc\alpha^2}{2h},\quad a_\infty=\frac{\alpha}{4\pi R_\infty}. \tag{A5}$$

Also, we take $\epsilon=E_{\rm SI}/E_A$, where the atomic unit of energy is

$$E_A({\rm J})=\left(\frac{m}{\mu}\right)\frac{\hbar^2}{ma^2}=2\left(\frac{m}{\mu}\right)hcR_\infty=2hcR_A, \tag{A6}$$

where R_∞ and R_A are in units of m^{-1}. Furthermore, $F=F_{\rm SI}/F_A$, where the atomic unit of field is

TABLE IV. Relevant fundamental constants used in obtaining the atomic units of energy and field in the Appendix. All values are taken from Ref. [59].

Constant	Value	Units
e	$1.60217733(49)\times10^{-19}$	Coulomb
c	2.99792458×10^{8}	m/sec
α^{-1}	137.0359895(61)	
a_∞	$5.29177249(24)\times10^{-11}$	m
m	$9.1093897(54)\times10^{-31}$	kg
u	$1.6605402(10)\times10^{-27}$	kg

$$F_A(\mathrm{V/m})=\frac{\hbar^2}{\mu e a^3}=\frac{1}{a^2}\left(\frac{e\mu_0 c^2}{4\pi}\right)=\frac{10^{-7}ec^2}{a^2}$$
$$=\left(\frac{\mu}{m}\right)^2\frac{10^{-7}ec^2}{a_\infty^2}. \tag{A7}$$

In summary, the atomic mass-dependent effects may be summarized as follows:

$$a=a_\infty/\rho_A,\quad E_A=E_\infty\rho_A,\quad F_A=F_\infty\rho_A^2, \tag{A8}$$

where

$$\rho_A=\frac{\mu}{m}=\frac{M}{M+m}=\frac{M_A-m}{M_A}=1-\frac{m}{M_A}. \tag{A9}$$

M_A is normally stated in terms of the atomic mass unit: $M_A=Au$. Using the 1986 recommended values of m and u from Table IV, we obtain

$$\rho_A=1-\frac{5.485\,799(5)\times10^{-4}}{A}. \tag{A10}$$

For the Rydberg constant for an atom with infinite nuclear mass R_∞, the weighted average of two recent experimental results [56,57] provides higher accuracy than we need:

$$R_\infty=109\,737.315\,683\,7(31)\ \ \mathrm{cm}^{-1}. \tag{A11}$$

The atomic unit of electric field for infinite nuclear mass, $F_\infty=e/a_\infty^2$ in Gaussian units or $10^{-5}ec^2/a_\infty^2$ V/cm, is obtained from the fundamental constants listed in Table IV:

$$F_\infty=5.142\,208\,3(16)\times10^{9}\ \ \mathrm{V/cm}. \tag{A12}$$

For ^{7}Li, $A=7.016\,004\,1(5)$ [58] and the reduced mass correction is

$$\rho_{^7\mathrm{Li}}=1-7.818\,979(8)\times10^{-5} \tag{A13}$$

and therefore

$$R_{^7\mathrm{Li}}=R_\infty\rho_{^7\mathrm{Li}}=109\,728.735\,35(1)\ \ \mathrm{cm}^{-1},$$

$$F_{^7\mathrm{Li}}=F_\infty\rho_{^7\mathrm{Li}}^2=5.141\,404\,2(16)\times10^{9}\ \ \mathrm{V/cm}.$$

[1] D.-H. Yang, D. Lieberman, P. van der Straten, T. Bergeman, and H. Metcalf, Phys. Rev. A **40**, 5026 (1989).
[2] M. Ciocca, C. Burkhardt, J. J. Leventhal, and T. Bergeman, Phys. Rev. A **45**, 4720 (1992).
[3] G. Stevens, C.-H. Iu, S. Williams, T. Bergeman, and H. Metcalf, Phys. Rev. A **51**, 2866 (1995).
[4] G. Alvarez, R. Damburg, and H. J. Silverstone, Phys. Rev. A **44**, 3060 (1991).
[5] E. Luc-Koenig and A. Bachelier, J. Phys. B **13**, 1743 (1980); **13**, 1769 (1980).
[6] H. J. Silverstone, Phys. Rev. A **18**, 1853 (1978).
[7] A. Nussenzweig, E. Eyler, T. Bergeman, and E. Pollack, Phys. Rev. A **41**, 4944 (1990).
[8] S. Feneuille, S. Liberman, E. Luc-Koenig, J. Pinard, and A. Taleb, J. Phys. B **15**, 1205 (1982).
[9] C. Chardonnet, D. Delande, and J.-C. Gay, Opt. Commun. **51**, 249 (1984).
[10] J.-Y. Liu, P. McNicholl, D. A. Harmin, J. Ivri, T. Bergeman, and H. Metcalf, Phys. Rev. Lett. **55**, 189 (1985).
[11] P. McNicholl, T. Bergeman, and H. Metcalf, Phys. Rev. A **37**, 3302 (1988).
[12] D. A. Harmin, Phys. Rev. A **24**, 2491 (1981).
[13] D. A. Harmin, Phys. Rev. A **26**, 2656 (1982).
[14] D. A. Harmin, Phys. Rev. A **30**, 2413 (1984).
[15] C.-H. Iu, G. Welch, M. Kash, D. Kleppner, D. Delande, and J. C. Gay, Phys. Rev. Lett. **66**, 145 (1991).
[16] M. H. Halley, D. Delande, and K. T. Taylor, J. Phys. B **25,** L525 (1992).
[17] I. Seipp and K. T. Taylor, J. Phys. B **27,** 2785 (1994).
[18] M. H. Halley, D. Delande, and K. T. Taylor, J. Phys. B **26,** 1775 (1993).
[19] G. D. Stevens *et al.*, Phys. Rev. Lett. **75**, 3402 (1995).
[20] M. Zimmerman, M. Littman, M. Kash, and D. Kleppner, Phys. Rev. A **20**, 2251 (1979).
[21] D. Delande, K. T. Taylor, M. H. Halley, T. van der Veldt, W. Vassen, and W. Hogervorst, J. Phys. B **27,** 2771 (1994).
[22] C. H. Iu, G. Stevens, and H. Metcalf, Appl. Opt. **34**, 2640 (1995).
[23] P. McNicholl, J. Ivri, and T. Bergeman (unpublished).
[24] P. McNicholl, T. Bergeman, and H. Metcalf, in *Spectral Line Shapes*, edited by R. J. Exton (Deepak, Hampton, VA, 1987), Vol. 4.
[25] R. J. Drachman and A. K. Bhatia, Phys. Rev. A **51**, 2926 (1995).

[26] W. Ritz, Phys. Z. **4**, 406 (1903).
[27] D. Hartree, Proc. Cambridge Philos. Soc. **24**, 426 (1928).
[28] G. W. F. Drake and R. Swainson, Phys. Rev. A **44**, 5448 (1991).
[29] G. Drake, *Advances in Atomic, Molecular, and Optical Physics*, edited by D. Bates and B. Bederson (Academic, New York, 1993), Vol. 31, p. 1; (1994), Vol. 32, p. 93.
[30] N. Rothery, C. Storry, and E. Hessels, Phys. Rev. A **51**, 2919 (1995).
[31] C. J. Sansonetti, B. Richou, R. Engleman, Jr., and L. Radziemski, Phys. Rev. A **52**, 2682 (1995).
[32] L. J. Radziemski, R. Engleman, Jr., and J. W. Brault, Phys. Rev. A **52**, 4462 (1995).
[33] I. Johansson, Ark. Fys. **15**, 169 (1959).
[34] P. Goy, J. Liang, M. Gross, and S. Haroche, Phys. Rev. A **34**, 3889 (1986).
[35] W. Cooke, T. Gallagher, R. Hill, and S. Edelstein, Phys. Rev. A **16**, 1141 (1977).
[36] C.-H. Iu, M. Kash, G. Welch, and D. Kleppner (unpublished).
[37] E. Schrödinger, Ann. Phys. (Leipzig) IV **80**, 29 (1926).
[38] B. Numerov, Publ. Observ. Astrophys. Central Russie **2**, 188 (1933).
[39] S. Bhatti, C. Cromer, and W. Cooke, Phys. Rev. A **24**, 161 (1981).
[40] D. Bates and A. Damgaard, Philos. Trans. R. Soc. London **242**, 101 (1949).
[41] W. Gordon, Ann. Phys. (Leipzig) **2**, 1031 (1929).
[42] H. A. Bethe and E. E. Salpeter, *Quantum Mechanics of One- and Two-Electron Atoms* (Springer, Berlin, 1957).
[43] A. R. Ruffa, Am. J. Phys. **41**, 234 (1973).
[44] H. J. Silverstone (private communication).
[45] A. R. Edmonds, *Angular Momentum in Quantum Mechanics* (Princeton University Press, Princeton, NJ, 1960).
[46] M. J. Seaton, Rep. Prog. Phys. **46,** 167 (1983)
[47] A. Alijah, J. T. Broad, and J. Hinze, J. Phys. B **19**, 2617 (1986).
[48] B. I. Schneider, Phys. Rev. A **24,** 1 (1981).
[49] M. E. Rose, *Elementary Theory of Angular Momentum* (Wiley, New York, 1957).
[50] D. Delande *et al.* (unpublished).
[51] A. Buchleitner, B. Grémaud, and D. Delande, J. Phys. B **27,** 2663 (1994).
[52] W. H. Press, S. A. Teukolsky, W. T. Vetterling and B. P. Flannery, *Numerical Recipes in Fortran* (Cambridge University Press, Cambridge, England, 1992).
[53] S. Themelis and C. Nicolaides, Phys. Rev. A **51**, 2801 (1995).
[54] J. E. Bjorkholm and P. F. Liao, Phys. Rev. A **14**, 751 (1976).
[55] T. Bergeman (unpublished).
[56] F. Nez, M. Plimmer, S. Bourzeix, L. Julien, F. Biraben, R. Felder, O. Acef, J. Zondy, P. Laurent, A. Clairon, M. Abed, Y. Millerioux, and P. Juncar, Phys. Rev. Lett. **69**, 2326 (1992).
[57] M. Weitz, A. Huber, F. Schmidt-Kaler, D. Leibfried, and T. Hänsch, Phys. Rev. Lett. **72**, 328 (1994).
[58] G. Audi and A. Wapstra, Nucl. Phys. **A565**, 1 (1993).
[59] E. R. Cohen and B. N. Taylor, Rev. Mod. Phys. **57**, 1121 (1987); B. N. Taylor and E. R. Cohen, J. Res. Natl. Inst. Stand. Technol. **95**, 497 (1990).